Feng *et al. Microstructures* **2025**, *5*, 2025068
DOI: 10.20517/microstructures.2024.115

Microstructures

Review

Open Access

Check for updates

Unraveling metastable perovskite oxides insights from structural engineering to synthesis paradigms

Yutong Feng[#], Jiao Dai[#], Mingjie Wang[#], Wanting Ding, Hanyuan Zhang, Weilin Xu, Jun Wan

State Key Laboratory of New Textile Materials and Advanced Processing Technologies, School of Chemistry and Chemical Engineering, Wuhan Textile University, Wuhan 430200, Hubei, China.
[#]These authors contributed equally to the work.

Correspondence to: Prof. Jun Wan, State Key Laboratory of New Textile Materials and Advanced Processing Technologies, Wuhan Textile University, 1 Sunshine Avenue, Jiangxia District, Wuhan 430200, Hubei, China. E-mail: wanj@wtu.edu.cn

How to cite this article: Feng, Y.; Dai, J.; Wang, M.; Ding, W.; Zhang, H.; Xu, W.; Wan, J. Unraveling metastable perovskite oxides insights from structural engineering to synthesis paradigms. *Microstructures* **2025**, *5*, 2025068. https://dx.doi.org/10.20517/microstructures.2024.115

Received: 8 Nov 2024 **First Decision:** 10 Dec 2024 **Revised:** 30 Dec 2024 **Accepted:** 13 Jan 2025 **Published:** 13 Jun 2025

Academic Editors: Shiqing Deng, Rongkun Zheng **Copy Editor:** Shu-Yuan Duan **Production Editor:** Shu-Yuan Duan

Abstract

Metastable perovskite oxides, with their complex atomic arrangements and nonequilibrium electronic structures, show great potential in fields such as energy conversion, storage, advanced optoelectronics, and intelligent sensing. Compared to conventional perovskites, metastable structures exhibit unique local symmetry breaking and oxygen vacancy modulation, high defect concentrations and tunable electronic structures. These features provide significant advantages in enhancing interfacial catalytic activity, ion transport, and photoelectric performance. However, their nonequilibrium structures tend to transform into more thermodynamically stable phases under typical synthesis conditions, complicating the study of their structure-property relationships and synthesis. This review adopts a structural materials perspective to analyze the unique advantages and structure-performance correlations of metastable perovskite oxides. Key concepts are introduced, categorizing these oxides based on their structural characteristics into four groups: symmetry-distorted type, Heterojunction type, Layered type, and Multivalent-regulated type, focusing on their impact on physicochemical properties. Major synthesis strategies, such as solid-state synthesis, high-pressure synthesis, pulsed laser deposition, salt-assisted method, and wet chemical approach, are systematically reviewed, highlighting their effectiveness in stabilizing metastable phases. The review also summarizes recent advancements in metastable perovskites, encompassing their types, structural features, synthesis methods, and applications, while identifying key challenges and future prospects in energy and information technologies.

Keywords: Metastable material, perovskite oxide, nonequilibrium structure, structural engineering, synthetic strategy

INTRODUCTION

Metastable perovskite oxides, as an emerging class of materials, exhibit unprecedented application potential in energy conversion[1], optoelectronic devices[2], and sensing technologies[3] due to their complex crystal structures and nonequilibrium electronic properties. These materials, through unique atomic arrangements and defect engineering[4] - such as local symmetry breaking, oxygen vacancy regulation[5], and high defect concentration - demonstrate exceptional performance in key aspects such as charge transport[6], interfacial catalysis[7], and optoelectronic response. Compared to thermodynamically stable perovskites[8], metastable materials exhibit greater structural flexibility, allowing researchers to manipulate their properties within a broader chemical space, endowing them with highly tunable electronic structures[9,10]. This flexibility arises from their sensitivity to local structural distortions and significant band structure reconstruction capabilities[11], making them highly promising in cutting-edge fields such as photocatalysis[12], electrochemical energy storage[13], and ion conduction[14]. Particularly in electrocatalytic reactions, the polarization effects induced by local symmetry breaking significantly improve charge separation efficiency, thereby enhancing interfacial catalytic activity. Oxygen vacancies further modify adsorption energy and reaction pathways, boosting the selectivity and kinetics of catalytic processes. Additionally, the tunable electronic structure driven by high defect concentrations enables these materials to optimize their electrical and optical performance within specific energy windows[15,16]. Thus, metastable perovskite oxides not only exhibit outstanding functional potential, but their unique structural regulation also provides a theoretical foundation for the development of new materials[17,18]. As materials science advances, in-depth analysis of these structural characteristics and their physicochemical mechanisms will be crucial in revealing the performance advantages of metastable perovskites, establishing a new paradigm for research in this field.

The diversity of metastable perovskite oxides is primarily reflected in their rich crystal structures and multidimensional tunability[19-21]. Based on differences in crystal symmetry breaking, ionic occupancy, and electronic states, these materials can be categorized into four main types: local symmetry-distorted, heterojunction, layered, and multivalent-controlled structures. Local symmetry-distorted materials manipulate asymmetric stress within the crystal lattice to disrupt traditional crystalline symmetry, thereby regulating charge distribution and transport, which significantly enhances electrocatalytic activity[22-24]. Heterojunction structures, by constructing interfaces between different crystalline phases, improve photogenerated charge separation efficiency and provide more active sites for reaction processes[25]. The weak interlayer interactions in layered structures allow for more efficient ion conductivity, showing great potential in applications such as batteries and solid-state electrolytes[26,27]. Multivalent-controlled structures, through the dynamic coexistence of multiple oxidation states, impart stronger charge transfer capabilities and reaction flexibility to the materials[28]. While the structural diversity of these metastable perovskites is crucial for functional materials, it also presents significant synthesis challenges. The formation of metastable perovskites often relies on highly precise control conditions, such as high temperatures, high pressures, and rapid quenching, making it difficult for traditional synthesis strategies to maintain phase stability under these stringent conditions[29,30]. Current research has focused primarily on optimizing performance[31], but systematic studies on the formation mechanisms of metastable structures and their synthesis methods remain insufficient. Especially in understanding how structures form and how synthesis methods affect their final performance, there is a need for further exploration and breakthroughs[32,33]. Therefore, systematically analyzing the structural formation of metastable perovskites and their synthesis mechanisms is essential for uncovering their performance regulation mechanisms[34,35].

This review aims to systematically examine the structural characteristics of metastable perovskite oxides and their interactions with synthesis methods, while exploring their potential in advanced functional materials. As shown in Figure 1, the basic concepts of metastable perovskite oxides and their unique structural types

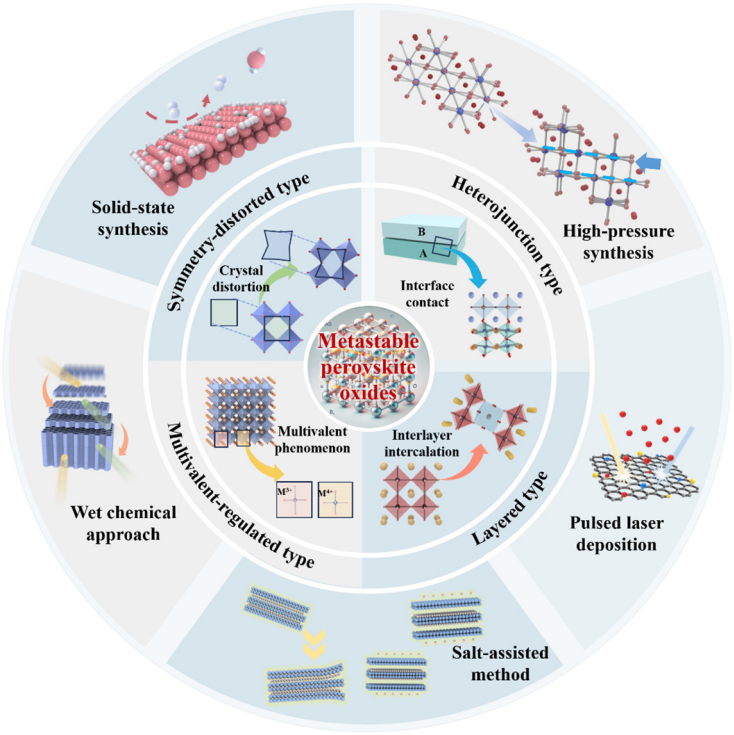

Figure 1. Overview of the classification and synthesis techniques of metastable perovskite oxides.

will be thoroughly analyzed, with a focus on the physicochemical properties of four major structural categories: symmetry-distorted type, Heterojunction type, Layered type, and Multivalent-regulated type, and their impact on material performance. Subsequently, the review will systematically summarize the widely applied synthesis strategies, analyzing the advantages and limitations of various methods in structural regulation and discussing how these approaches influence the formation mechanisms and final performance of the materials. Unlike other reviews, this study not only focuses on the relationship between structure and performance but also delves deeply into the interaction between synthesis methods and material structures, revealing the critical role of synthesis strategies in material design. By systematically analyzing the interplay between structural regulation and synthesis mechanisms, this review aims to provide theoretical support and practical guidance for future research on metastable perovskite oxides. Finally, the review will discuss the future challenges and opportunities in this field, focusing on how the synergistic optimization of structure and synthesis can drive the application of metastable perovskite oxides in high-performance material development, offering new research avenues for future material design.

STRUCTURAL ANALYSIS OF METASTABLE PEROVSKITE OXIDES

Metastable perovskite oxides exhibit complex atomic configurations that depart significantly from their thermodynamically stable counterparts. This nonequilibrium nature opens up unique pathways for tailoring properties that are critical in fields such as energy conversion, advanced catalysis, and next-generation electronics[36,37]. The ability to control metastable phases, stabilize them, and exploit their structure-property relationships lies at the heart of current materials research. This section delves into the fundamental structural principles underlying metastable perovskite oxides, explores their classification based on structural features, and analyzes how these features contribute to enhanced performance in key applications.

Concept of metastable perovskite oxides

Metastability results from the balance between thermodynamics and kinetics, where **metastable states** lie between stable and unstable phases with distinct energy levels[38]. As shown in Figure 2A, metastable materials are thermodynamically less stable but can persist under controlled external conditions such as temperature, pressure, or chemical potential. Stable phases represent the lowest-energy state of the system, while unstable phases exist at higher energies, transitioning rapidly to stability. Transient states, lasting nanoseconds to microseconds, mediate transitions between metastable and stable phases. Metastable perovskite oxides, stabilized under specific synthesis conditions, retain high-energy configurations, offering unique electronic, optical, and magnetic properties not found in stable phases. This nonequilibrium state is valuable for applications requiring high reactivity, tunable electronic structures, and enhanced ion transport.

A key feature of metastable perovskite oxides is their structural flexibility, driven by symmetry distortions during synthesis. Incorporating cations of varying ionic radii or applying external stimuli alters the ideal cubic or tetragonal structure, causing octahedral tilting or bond angle distortions. These deviations significantly influence electronic properties such as optical absorption[39,40]. Changes in BO_6 octahedral bond angles affect the bandgap and light absorption[41], making metastable perovskites ideal for optoelectronic applications requiring precise bandgap tuning[42]. High defect concentrations, especially oxygen vacancies, enhance charge transfer and catalytic activity. Oxygen vacancies, reaching up to 10^{21} cm^{-3}[43], improve ionic conductivity and reactivity, critical for catalytic processes such as oxygen evolution reactions (OER). Oxygen vacancies promote OER by facilitating oxygen ion diffusion and enhancing catalytic activity. The structural flexibility of metastable perovskites enables fine-tuning of oxygen vacancy concentration and ordering, optimizing OER performance and making them promising candidates for efficient catalytic processes[44].

Despite their promising properties, metastable perovskites face significant challenges due to inherent instability[45,46]. Under typical conditions, these materials tend to revert to their stable phases, especially at elevated temperatures or over extended use[47]. Transient states, short-lived high-energy configurations, play a key role in the evolution of metastable phases[48,49]. For example, Makovec *et al.* synthesized $Bi_4Ti_5O_{12}$ nanowires (15-35 nm in width, several micrometers in length) via controlled hydrothermal synthesis, showing that the nanowire structure remains metastable and preserves ferroelectric (FE) properties below 500 °C[50]. Kim *et al.* developed a low-temperature (300-500 °C) method for $LaFeO_3$ perovskite, using a cyanogel-peroxide complex as a metastable precursor. The resulting catalyst exhibited excellent OER performance (438 mV @ 100 mA/cm^2) and long-term stability (< 1% degradation over 50 h)[51]. O'Donnell *et al.* synthesized metastable Cu(I)-based semiconductors, Cu_2SnO_3 and $Cu_{2-x}Li_xTiO_3$, through cation exchange at 475 °C, obtaining excellent bandgap tuning (as low as 1.46 eV) and carrier transport properties (effective electron mass of 0.41 m_e)[52]. Metastable perovskites exhibit enhanced structural flexibility and tunable properties compared to traditional perovskites and metal-organic frameworks (MOFs). Unlike conventional perovskites, which stabilize in a single phase, metastable perovskites can adopt multiple structures, improving electronic, ionic, and catalytic performance. This tunability makes them ideal for applications in energy storage and catalysis. In contrast to MOFs, which excel in gas storage, metastable perovskites offer greater thermal and chemical stability, making them suitable for high-performance environments[53]. To stabilize these materials, precise synthesis control is essential to prevent phase transitions. By balancing thermodynamics and kinetics, researchers aim to harness the unique properties of metastable perovskites for catalytic, electronic, and energy storage applications[54].

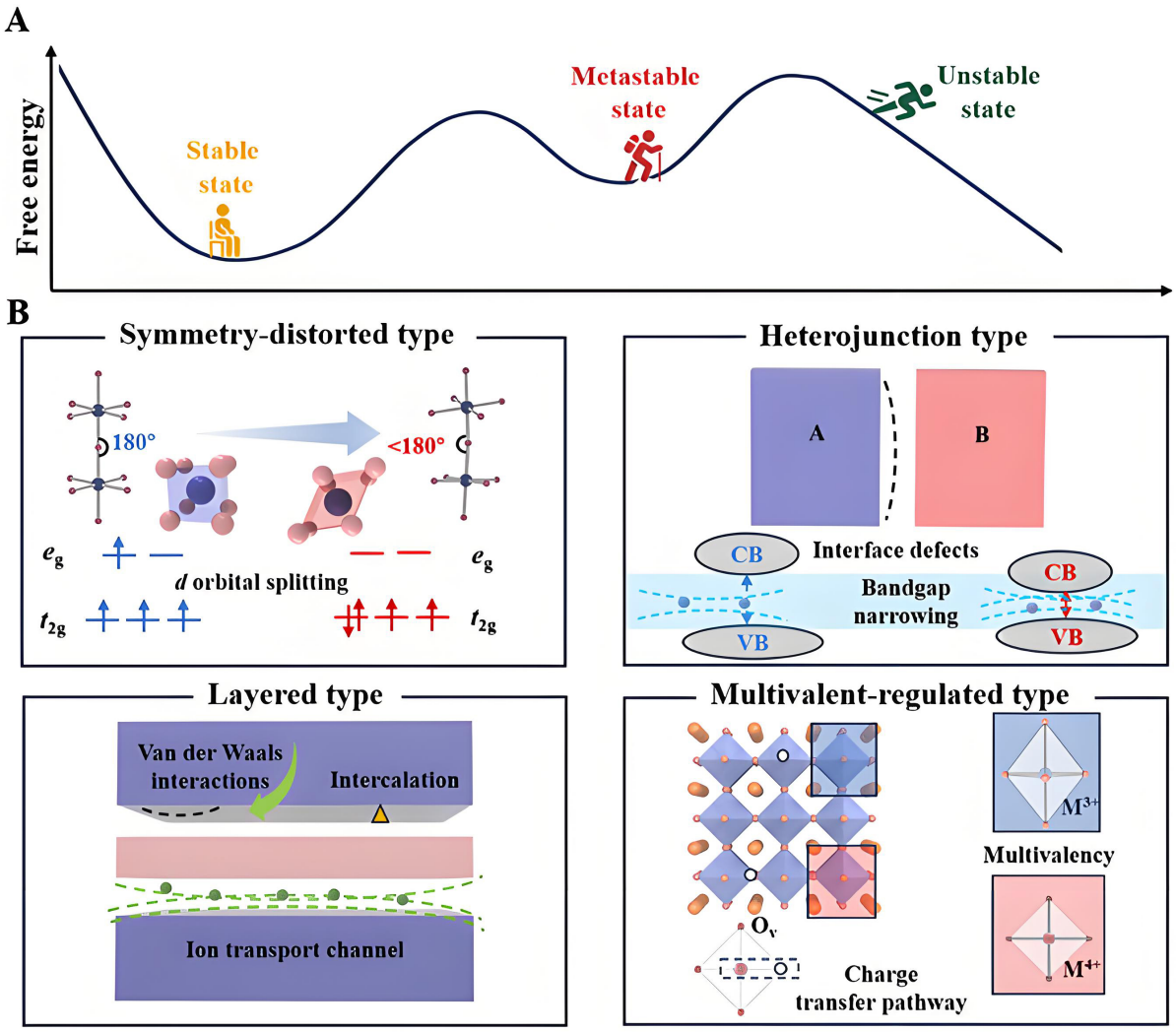

Figure 2. (A) Schematic illustrating free energy profiles for transitions among metastable, unstable, and stable states within phase space; (B) Structural characteristics of various metastable perovskite oxide types.

Classification of metastable perovskite oxides

Metastable perovskite oxides can be classified into four main structural types based on symmetry deviation and their resulting physical properties [Figure 2B]: symmetry-distorted, heterojunction, layered, and multivalent-regulated structures. Each type offers unique advantages in catalysis, energy storage, and electronics. The following sections explore these classifications, focusing on structural features and performance metrics.

Symmetry-distorted type

Symmetry-distorted metastable perovskites deviate from ideal lattice configurations, altering their electronic and optical properties. These distortions arise from factors such as cation substitution with varying ionic radii or external stresses during synthesis. Such asymmetries disrupt cubic or tetragonal symmetry, causing bond angle shifts and octahedral tilting. For example, B-O-B bond angles in BO_6 octahedra deviate from 180°, tilting by a few degrees, which modifies the electronic band structure[55]. Jahn-Teller distortions further split the *d*-orbitals of transition metals, narrowing the bandgap and enhancing light absorption and charge

separation in photocatalytic systems[56]. Jahn-Teller distortions further split the *d*-orbitals of transition metals, narrowing the bandgap and enhancing light absorption and charge separation in photocatalytic systems[57]. Local polarization fields generated by distortions reduce electron-hole recombination and improve charge mobility, essential for photocatalytic water splitting and solar-driven reactions. The temperature dependence of these distortions creates a competition between static and dynamic effects, leading to complex changes in optoelectronic properties[58]. Additionally, these distortions improve dielectric properties, increasing charge storage capacity. The tunable nature of these distortions underscores their potential in optoelectronic and catalytic applications.

A compelling example of symmetry breaking induced by light reveals the tunability of symmetry-distorted perovskites. Nova *et al.* investigated the effect of optical excitation on strontium titanate [$SrTiO_3$ (STO)], a notable metastable perovskite oxide[59]. STO maintains a paraelectric, centrosymmetric structure and undergoes an antiferrodistortive transition from cubic to tetragonal at 105 K [Figure 3A]. Under mid-infrared optical pulses, lattice deformations induce a metastable polar-ordered phase, stable for hours even above 290 K [Figure 3B]. This underscores the potential of metastable phases and the discovery of "hidden phases" with novel functionalities. For example, Li *et al.* demonstrated an ultrafast phase transition to a hidden FE phase in quantum paraelectric STO using intense terahertz electric field excitation[60]. By applying a single-cycle THz electric field to drive the "soft" lattice mode, collective ionic displacements transitioned STO from a high-symmetry paraelectric state to a lower-symmetry configuration with a dipole moment, promoting a long-range FE crystalline phase [Figure 3C]. This precise control over ferroelectricity points to promising applications in memory devices.

Building on insights into STO, Kim *et al.* examined oxygen octahedral rotation (OOR) in perovskite oxides[61]. While the $a^-b^+a^-$ OOR pattern [Figure 3D] dominates at equilibrium, it limits functionality. Kim *et al.* stabilized a metastable $a^-a^-a^-$ OOR pattern [Figure 3E]in $CaTiO_3$ through heteroepitaxial growth on a $LaAlO_3$ (LAO) (111) substrate [Figure 3F], optimizing octahedral connectivity and enabling potential room-temperature ferroelectricity. Kawamoto *et al.* synthesized a metastable $LiNbO_3$-type $ScFeO_3$ from orthorhombic perovskite under 15 GPa and high temperature[62]. Neutron diffraction and high-angle annular dark-field scanning transmission electron microscopy (HAADF-STEM) [Figure 3G] confirmed the polar R3c symmetry [Figure 3H]. Sc and Fe ions are in highly distorted ScO_6 and FeO_6 octahedra. Despite limitations, HAADF-STEM images support the $LiNbO_4$-type structure over corundum. Synchrotron X-ray diffraction (SXRD) [Figure 3I] revealed adjacent Sc and Fe sites along the c-axis in a face-sharing octahedral configuration [Figure 3J]. The $LiNbO_4$-type phase is denser than the corundum phase, with a density of 4.513 g cm^{-3}.

Building upon the exploration of symmetry distortions in perovskite structures, Zhang *et al.* characterized FeO_6 octahedral distortions in $La_{1-x}Ce_xFeO_3$ (x = 0, 0.25, 0.5, 0.75, 1) orthorhombic perovskites, showing how Ce^{3+} substitution affects Fe-O bond length variations[63]. Electrical conductivity relaxation and density functional theory (DFT) calculations revealed that these variations modulate FeO_6 octahedral distortion. Figure 4A illustrates the distortions, with $La_{0.5}Ce_{0.5}FeO_3$ showing the greatest bond length variance and the highest octahedral distortion [Figure 4B]. These findings suggest that metastable perovskite oxides can enhance oxygen mobility, benefiting catalysis and energy conversion technologies. In a parallel study, Gabilondo *et al.* synthesized the distorted Sn(II)-perovskite oxide $SnHfO_3$ (o-SHO) through a low-temperature ion-exchange approach[64]. This approach reacted orthorhombic $PbHfO_3$ (o-PHO) with SnClF to yield o-SHO and PbClF as a by-product [Figure 4C]. Structural analysis revealed significant octahedral tilting and A-site distortions, each stabilizing the structure by approximately 30 meV per atom. However, the barriers for structural rearrangement exceeded those for decomposition into SnO and HfO_2. Figure 4D

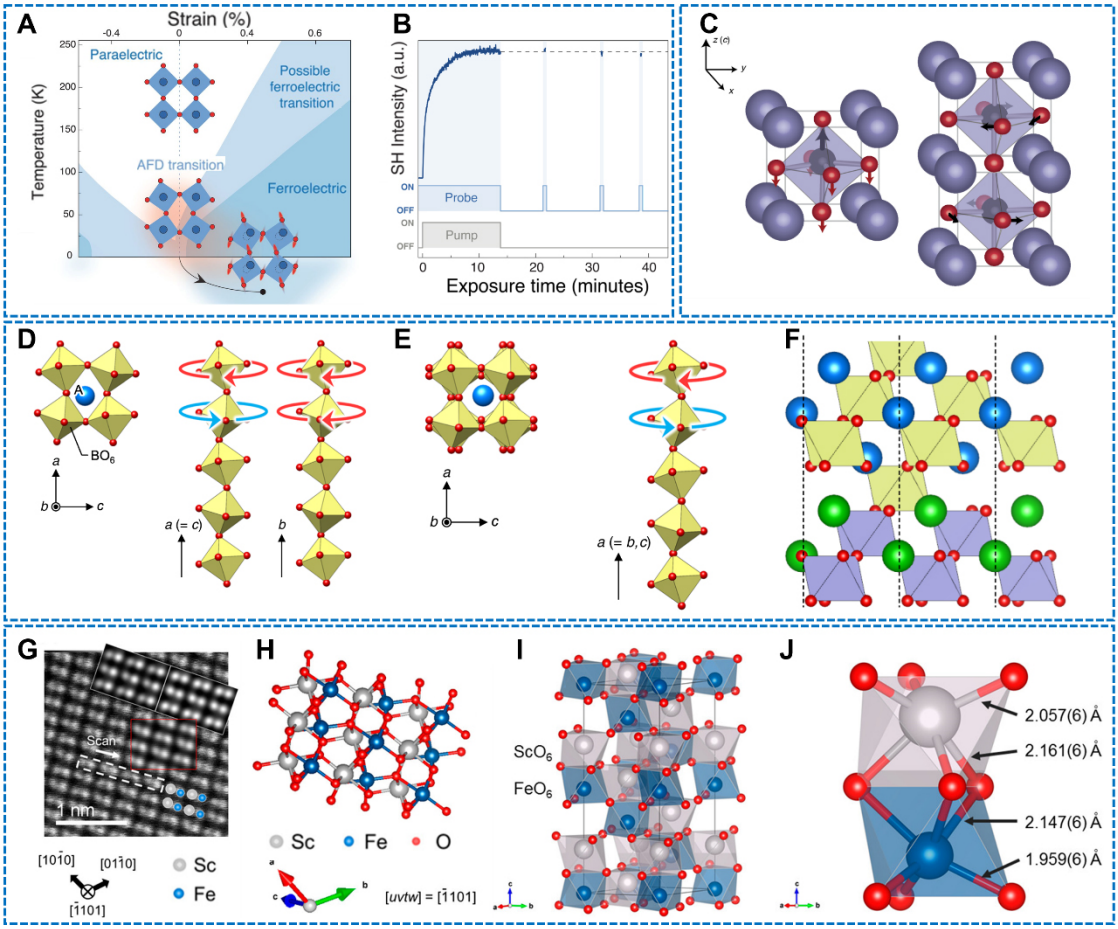

Figure 3. (A) Antiferrodistortive transition of $SrTiO_3$ from cubic to tetragonal phase; (B) Metastable phase second harmonic intensity with time after mid-infrared illumination. This figure is quoted with permission[59]; (C) Schematic of the phonon mode in STO. This figure is quoted with permission[60]; (D) Atomic structure of the $a^-b^+a^-$ OOR pattern in an ABO_3 perovskite; (E) Atomic structure of the $a^-a^-a^-$ OOR pattern in an ABO_3 perovskite; (F) Engineering of the OOR patterns between $a^-b^+a^-$ and $a^-a^-a^-$ structures in $CaTiO_3$. This figure is quoted with permission[61]; (G) HAADF-STEM image projection of $ScFeO_3$ under 15 GPa and at 1,450 °C; (H) Schematic of the $LiNbO_3$-type crystal structure of $ScFeO_3$; (I) Polyhedral schematic of the $LiNbO_3$-type $ScFeO_3$ crystal structure; (J) Local coordination structure of face-sharing ScO_6 and FeO_6 octahedra stacked along the c-axis. This figure is quoted with permission[62]. STO: $SrTiO_3$; OOR: oxygen octahedral rotation; HAADF-STEM: high-angle annular dark-field scanning transmission electron microscopy.

and E shows activation energy barriers based on decomposition rates, while total energy calculations outline the conditions for synthesizing various $SnHfO_3$ polymorphs. Remarkably, o-SHO undergoes reversible phase transitions to higher symmetries at Curie temperatures of 130 °C and 200 °C [Figure 4F].

Recent advances in chemical interception have enabled the study of metastable phases under varying pressures [Figure 4G]. Zhao *et al.* synthesized a metastable phase of Li_2TiTeO_6 with an ordered R3 ilmenite structure via topotactic ion exchange [Figure 4H][65]. This phase undergoes an irreversible first-order transition to the α-phase (Pnn2) above 560 °C, with enhanced second harmonic generation (SHG) intensity. These findings demonstrate the effectiveness of topotactic chemical interception in stabilizing metastable perovskite oxides. In a related investigation, Zhao *et al.* developed an extensive pipeline for the study of metastable phases, integrating data mining, high-throughput calculations, experimental synthesis, and chemical interception, using the nonmagnetic double-perovskite-related $Li_2B_4B'_6O_6$ as a model system[66]. Convex hull screening identified 140 compounds [Figure 4I], leading to the selection of Li_2TiWO_6 and

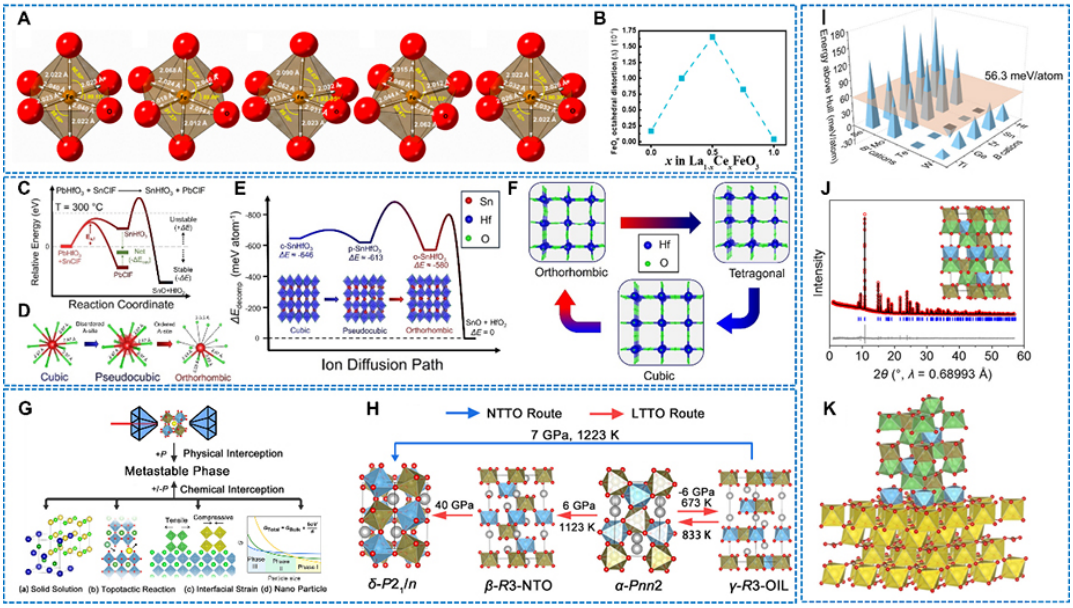

Figure 4. (A) Structural representations of $LaFeO_3$ and Ce-doped derivatives ($La_{0.75}Ce_{0.25}FeO_3$, $La_{0.5}Ce_{0.5}FeO_3$, $La_{0.25}Ce_{0.75}FeO_3$, and $CeFeO_3$) highlighting the FeO_6 octahedral framework; (B) Calculated FeO_6 octahedral distortion parameters for $LaFeO_3$ and Ce-doped variants; (C) Schematic of ion-exchange synthesis for $SnHfO_3$ using SnClF as the precursor. This figure is quoted with permission[63]; (D) Illustration of ion diffusion-induced symmetry reduction and structural tilting in $SnHfO_3$; (E) A-site distortion diagram showcasing the structural rearrangement in $SnHfO_3$; (F) Rietveld refinement pattern demonstrating the phase transition behavior in $SnHfO_3$. This figure is quoted with permission[64]; (G) Overview of four chemical strategies to intercept metastable phases; (H) Phase transition pathway analysis between NTTO and LTTO phases. This figure is quoted with permission[65]; (I) Convex hull analysis for phase stability based on formation energy. (J) Structural refinement of HP-LTTO phase; (K) Stabilization mechanism for HP-LTTO thin films on $CaCO_3$ substrate, with detailed octahedral structures of LiO_6 (green), TeO_6 (blue), TeO_6 (brown), and CaO_6 (yellow), and spherical representations for carbon (brown) and oxygen (red) atoms. This figure is quoted with permission[66].NTTO: Na_2TiTeO_6; HP-LTTO: high-pressure synthesis of Li_2TiTeO_6.

Li_2TiTeO_6 for validation. High-pressure synthesis of Li_2TiTeO_6 (HP-LTTO) produced an orthorhombic Ni_3TeO_6-type structure [Figure 4J], similar to Li_2ZrTeO_6. Future work will focus on fabricating Ni_3TeO_6-type LTTO thin films on $CaCO_3$ substrates, advancing the understanding of metastable perovskites and their potential applications [Figure 4K].

Heterojunction type

Heterojunction metastable perovskites exhibit unique properties due to phase interactions within a single material, forming interfaces that enhance charge transfer and separation. The electronic structure mismatch at these interfaces creates band offsets and built-in electric fields, inhibiting charge recombination and promoting electron-hole separation. These band offsets enable efficient carrier separation and rapid charge movement with minimal energy loss[67]. Time-resolved spectroscopy often shows charge transfer times of just a few picoseconds, highlighting the efficiency of interfacial dynamics. These interfaces significantly enhance material performance, with charge separation efficiencies improving by over 50% in optimal configurations[68]. In metastable perovskites, heterojunctions also stabilize phases that would otherwise revert to thermodynamically stable forms. By modifying interface properties, phase transformation rates can be reduced by several orders of magnitude, prolonging the high-energy configurations and functional properties of metastable phases[69]. This stabilization mechanism ensures extended operational lifetimes, making heterojunctions critical for high-performance electronic and photocatalytic applications.

Octahedral rotation mismatches are key to stabilizing distinct phases in complex oxide systems. Gao *et al.* investigated the impact of octahedral rotation mismatch on $SrRuO_3$ (SRO) heterostructures, emphasizing how interfacial strain affects phase stability[70]. By growing 10 nm SRO films on STO and $GdScO_3$-buffered STO substrates, they found that octahedral rotation patterns significantly influence lattice symmetry. The lattice mismatch between these materials generates interfacial strain, directly affecting the stability of different rotational configurations. This strain-rotation coupling mechanism is key to understanding phase stability in such heterostructures. The $GdScO_3$ buffer facilitates epitaxial growth of tetragonal SRO, forming four distinct rotational domains [Figure 5A]. The rotation axes of both materials align in phase, modulating the structural and electronic properties [Figure 5B].

In a parallel investigation, Anderson *et al.* synthesized ultra-thin $SrIrO_3$ films capped with STO on (111) STO substrates using pulsed laser deposition (PLD) [Figure 5C][71]. Scanning transmission electron microscopy (STEM) imaging revealed distinct layering, contrasting with the monoclinic bulk phase of $SrIrO_3$ [Figure 5D]. SXRD confirmed three-fold symmetry in the heterostructure. The epitaxial strain at the $SrIrO_3$/STO interface stabilizes the metastable pseudocubic phase, demonstrating how interfacial strain controls phase stability. Detailed STEM analysis of a three-bilayer $SrIrO_3$ film capped with five bilayers of STO showed sharp interfaces and a stacking arrangement consistent with the STO substrate. The fast Fourier transform (FFT) diffraction pattern further clarified the symmetry of heterostructure [Figure 5E]. This work confirms the synthesis of metastable pseudocubic perovskite $SrIrO_3$ on (111) STO and lays the groundwork for exploring the electronic properties of these complex heterostructures. Further research on SRO and $LaCoO_3$ (LCO) heterostructures supports the central role of interfacial octahedral coupling in stabilizing metastable phases[72]. X-ray diffraction (XRD) and reflection high-energy electron diffraction (RHEED) data confirm successful two-dimensional growth and sharp interfaces [Figure 5F and G]. The rotation phase mismatch between bulk SRO and LCO [Figure 5H] highlights challenges in achieving rigid oxygen octahedral connectivity at the interface. In thin SRO films, rotation patterns adapt to minimize interface energy, whereas thicker films revert to the bulk orthorhombic structure, resulting in competition among various rotational configurations [Figure 5I]. These results emphasize the importance of interfacial engineering in modulating the properties of metastable perovskite oxide heterostructures.

Layered type

Layered metastable perovskites exhibit a unique two-dimensional structure, with alternating perovskite-like units and other atomic planes, where weak Van der Waals forces between layers enable efficient charge transfer and ion transport. The tunability of interlayer spacing through ion intercalation or chemical modification optimizes electronic and ionic transport pathways. Their weak interlayer bonding and structural flexibility provide mechanical stability under cycling conditions, while maintaining high ionic conductivity ($> 10^{-3}$ S cm^{-1}), a critical benchmark for solid-state batteries and fuel cells. These properties, along with high chemical stability in extreme conditions, make them ideal for energy storage and ion-transport devices[73]. The tunable interlayer spacing allows precise control of ionic pathways and charge mobility, enhancing performance in high-rate and cycling stability applications[74]. Additionally, their layered structure accommodates mechanical stress, maintaining integrity over extended cycles, further supporting their use in advanced solid-state electrolytes and catalytic systems where thermal and chemical stability are essential[75].

To highlight the versatility of synthesis techniques for layered metastable perovskites, Zhou *et al.* employ a low-temperature (around 350 °C) ion exchange method to synthesize metastable phosphors $ALa_{1-x}Ta_2O_7:xBi^{3+}$ (where A = K, Na), using $RbLa_{1-x}Ta_2O_7:xBi^{3+}$ as the precursor [Figure 6A][76]. The compound $Ala_{0.98}Ta_2O_7:0.02Bi^{3+}$ adopts a stable Dion-Jacobson-type two-dimensional layered perovskite

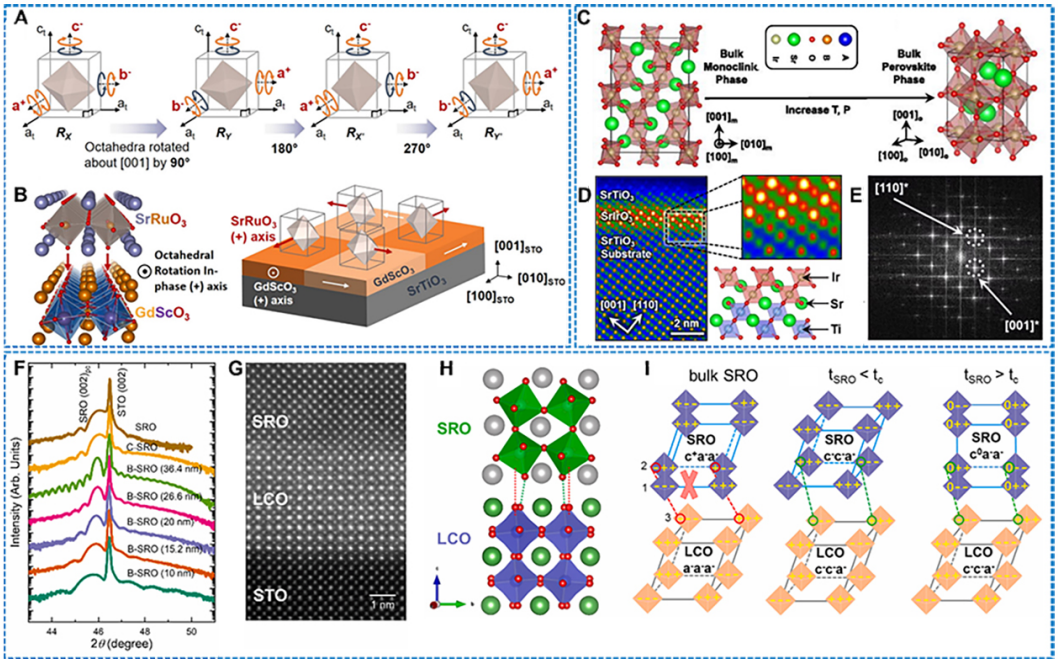

Figure 5. (A) Schematic of the four "rotational" domains (RX, RY, RX′, and RY′) in the tetragonal variant of $SrRuO_3$, where octahedra within the lattice rotate around the [001] axis by 0°, 90°, 180°, or 270°; (B) Tendency of the $SrRuO_3$ to align the in-phase (+) rotation axis with that of $GdScO_3$ during growth. This figure is quoted with permission[70]; (C) Structure of monoclinic $SrIrO_3$; (D) HAADF-STEM image of a 3-bilayer $SrIrO_3$ film capped with five bilayers of $SrTiO_3$; (E) FFT diffraction pattern indicating consistency of the $SrTiO_3$/$SrIrO_3$ heterostructure with the underlying $SrTiO_3$ substrate. This figure is quoted with permission[71]; (F) XRD 2θ-θ scan of SR heterostructures; (G) Cross-sectional HAADF image of B-SRO (20 nm); (H) Pseudocubic atomic model of SRO and LCO crystals; (I) Octahedral rotations between SRO and LCO represented using Glazer notation. This figure is quoted with permission[72]. HAADF-STEM: High-angle annular dark-field scanning transmission electron microscopy; FFT: fast Fourier transform; XRD: X-ray diffraction; SRO: $SrRuO_3$; LCO: $LaCoO_3$.

structure, demonstrating the effectiveness of topological chemical reactions in enhancing material properties. Additionally, Pravarthana *et al.* investigate $Dy_2Ti_2O_7$ (DTO) epitaxial thin films, stabilized in the monoclinic layered-perovskite phase using the Combinatorial Substrate Epitaxy (CSE) technique[77]. These films are deposited onto high-density DTO polycrystalline substrates [Figure 6B], which are stable in the monoclinic phase. As film thickness increases, a cubic pyrochlore phase emerges [Figure 6C], demonstrating the influence of substrate-induced phase selection. Microstructural analysis [Figure 6D and E] reveals the monoclinic structure with TiO_6 octahedral networks and intercalated O_2 layers. Shao *et al.* further explore the stability of $Ln_2Ti_2O_7$ (Ln = lanthanides) thin films, synthesized via sol-gel on (110)-oriented STO substrates[78]. While bulk LTO typically forms a layered-perovskite structure for Ln = La to Nd, thin films stabilize metastable (00l)-oriented layered-perovskite structures for $Sm_2Ti_2O_7$, $Eu_2Ti_2O_7$, and $Gd_2Ti_2O_7$. This is attributed to substrate-induced strain and favorable lattice matching. The study also notes a reduction in the ionic radii ratio (rLn^{3+}/rTi^{4+}) from 1.78 in bulk to 1.74 in thin films, influencing phase stability and the energy landscape [Figure 6F].

Extending this work, Shao *et al.* synthesize metastable $Sm_2Ti_2O_7$ thin films using the sol-gel method, stabilizing the monoclinic/layered perovskite structure on (110)-oriented STO substrates due to substrate-induced strain[79]. While $Sm_2Ti_2O_7$ typically crystallizes in a cubic/pyrochlore structure, it stabilizes as a monoclinic/layered perovskite when deposited on (110)-oriented STO substrates due to substrate-induced strain [Figure 6G]. This stabilized structure comprises two monoclinic cells, resulting in a centered orthogonal reciprocal subcell, as evidenced by the Selected Area Electron Diffraction pattern [Figure 6H and

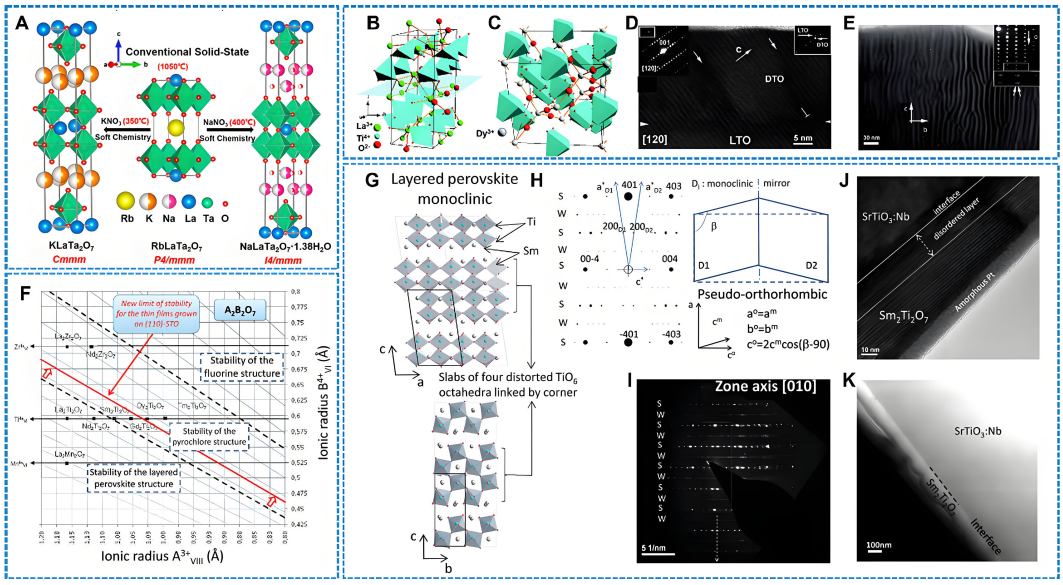

Figure 6. (A) Schematic illustration of the structural transformation process of the 2D-layered perovskite $ALaTa_2O_7$ (A = Rb, K, Na) through ion exchange. This figure is quoted with permission[76]; (B) Ball-and-stick model depicting the standard layered perovskite structure; (C) Schematic of the cubic pyrochlore structure; (D) Plan-view HRTEM image of the DTO film grown on the LTO substrate; (E) HRTEM image of the DTO film in the DTO/LTO interface region, with the corresponding cross-sectional selected area ED (SAED) pattern shown in the lower left corner and an enlarged ED image in the upper right corner. This figure is quoted with permission[77]; (F) Structural variations of $Ln_2Ti_2O_7$ compounds depending on the ionic radius ratio of the different cations $VIIIA^{3+}$ and VIB^{4+}. This figure is quoted with permission[78]; (G) Projections of the single-crystal $Sm_2Ti_2O_7$ along the [100] and [010] directions; (H) Calculated diffraction pattern and structural diagram of monoclinic twin crystals; (I) SAED pattern of single-crystal $Sm_2Ti_2O_7$; (J) Cross-sectional HR-TEM image of $Sm_2Ti_2O_7$; (K) STEM-HAADF image of $Sm_2Ti_2O_7$. This figure is quoted with permission[79]. HRTEM: High-Resolution transmission electron microscopy; SAED: selected area ED; ED: electron diffraction; DTO: $Dy_2Ti_2O_7$; LTO: $La_2Ti_2O_7$; STEM-HAADF:scanning transmission electron microscopy - high-angle annular dark field.

I]. High-Resolution Transmission Electron Microscopy (HRTEM) analysis of the cross-section reveals a film thickness of 90 ± 10 nm [Figure 6J], with substantial atomic weight of Sm enhancing the film-substrate interface visualization [Figure 6K]. The resulting (00l)-oriented SmTO phase is isostructural with monoclinic $Sm_2Ti_2O_7$ and exhibits properties comparable to the well-characterized $Sm_2Ti_2O_7$ family (Ln = La, Ce, Pr, Nd), highlighting the potential of layered perovskite structures in other compounds with smaller ionic radii.

Multivalent-regulated type

Multivalent-regulated metastable perovskites dynamically adjust oxidation states within their structure, offering flexibility in electronic and ionic behaviors. The coexistence of multiple oxidation states supports continuous redox cycling, enhancing electron mobility and catalytic efficiency, which is critical for reactions such as oxygen reduction and evolution[26]. This dynamic regulation optimizes charge transfer kinetics and surface reactivity, reducing electron transfer barriers and improving reaction rates. Oxygen vacancies further boost performance by increasing ionic conductivity and providing additional charge transport pathways. These vacancies act as active sites, facilitating ion migration and surface reactions, which enhance catalytic turnover. Modulating vacancy concentration allows control over electrical conductivity and ion mobility, key for energy storage and conversion. In batteries and fuel cells, the combination of multivalent flexibility and high vacancy concentrations supports high current densities with low overpotentials[28]. Moreover, dynamic oxidation state regulation ensures electrochemical stability under cycling conditions, maintaining performance over time. This balance of tunable electronic and ionic properties makes these perovskites ideal for next-generation energy devices requiring fast ion transport and efficient energy

conversion.

Visualizing oxygen vacancy distributions is critical to understanding their impact on material properties. Advanced electron microscopy techniques, such as HAADF-STEM, annular bright-field STEM (ABF-STEM), and electron energy-loss spectroscopy (EELS), provide complementary information for this purpose. HAADF-STEM reveals the cation sublattice structure, ABF-STEM directly images oxygen positions and vacancies, while EELS offers insights into the chemical states of transition metal elements influenced by vacancies. When combined with diffraction techniques such as XRD and neutron diffraction, which provide long-range structural data, these methods allow researchers to comprehensively understand oxygen vacancy ordering in multivalent metastable perovskites. Such insights are essential for correlating oxygen vacancy patterns with their effects on ionic conductivity, catalytic activity, and other functional properties.

Anionic doping presents a promising alternative to conventional cation doping strategies. Katsumata *et al.* introduce an electrochemical anionic doping technique for precise control over the type, rate, and extent of anion incorporation[80]. This method was demonstrated by fluorine (F) doping of $La_{0.5}Sr_{0.5}CoO_{3-\delta}$ perovskite oxide. ABF-STEM images reveal a highly crystalline structure in both surface and bulk regions, with R3c symmetry confirmed by FFT analysis [Figure 7A]. The low crystallinity observed in the surface layer of LSC55-F20 particles [Figure 7B] suggests a metastable phase. Advanced characterization, including time-of-flight secondary ion mass spectrometry (TOF-SIMS) and STEM EELS [Figure 7C], confirms fluorine incorporation at both the surface and bulk levels. These results show that electrochemical doping effectively modulates fluorine concentrations without inducing decomposition [Figure 7D and E], offering a new method to enhance energy materials such as catalysts, battery components, and fuel cell electrodes through anion defect engineering.

To further explore the impact of oxygen vacancy engineering on multivalent metastable perovskites, Liu *et al.* examine the metastable oxide $SrRuO_{3-\delta}$ ($SRO_{3-\delta}$) grown on (001)-oriented STO substrates via PLD [Figure 7F and G][81]. To promote a ferromagnetic Mott-insulating phase at the interface [Figure 7H], STO substrates were pre-annealed to create a high concentration of oxygen vacancies before film deposition. Additionally, exposing the STO substrates to light energy exceeding its optical bandgap (3.27 eV) induced charge transfer and orbital reconstruction at the $SRO_{3-\delta}$/STO interface, enabling optical modulation of the Mott insulator transition [Figure 7I]. The controlled manipulation of synthesis parameters offers Waidha *et al.* an alternative pathway in the development of novel materials, as demonstrated in their synthesis of a highly oxygen-deficient metastable perovskite-related phase, $BaCoO_{2+\delta}$ (where d is approximately 0.01-0.02)[82]. This phase was achieved by high-temperature reactions with brief heating, resulting in a defect-rich structure with Co^{2+} ions in partial square planar coordination - a rare environment for cobalt. Rietveld analysis of X-ray and neutron diffraction data indicated that all reflections correspond to a 2 × 2 × 1 tetragonally distorted superstructure of the cubic perovskite aristotype [Figure 7J]. Two structural models were examined [Figure 7K], with model #1 providing the best fit. Neither model showed full oxygen vacancy ordering, suggesting Co^{2+} ions in square planar or lower coordination states. This highly oxygen-deficient metastable phase forms despite the thermodynamically stable $BaCoO_2$ modifications, highlighting the unique properties and potential applications of multivalent metastable perovskite.

SYNTHETIC STRATEGIES FOR METASTABLE PEROVSKITE OXIDES

The synthesis of metastable perovskite oxides presents a complex challenge, as these materials inherently exist in nonequilibrium states that are often prone to transition into more thermodynamically stable phases[83]. A thorough understanding of the synthesis strategies and their limitations is crucial for stabilizing

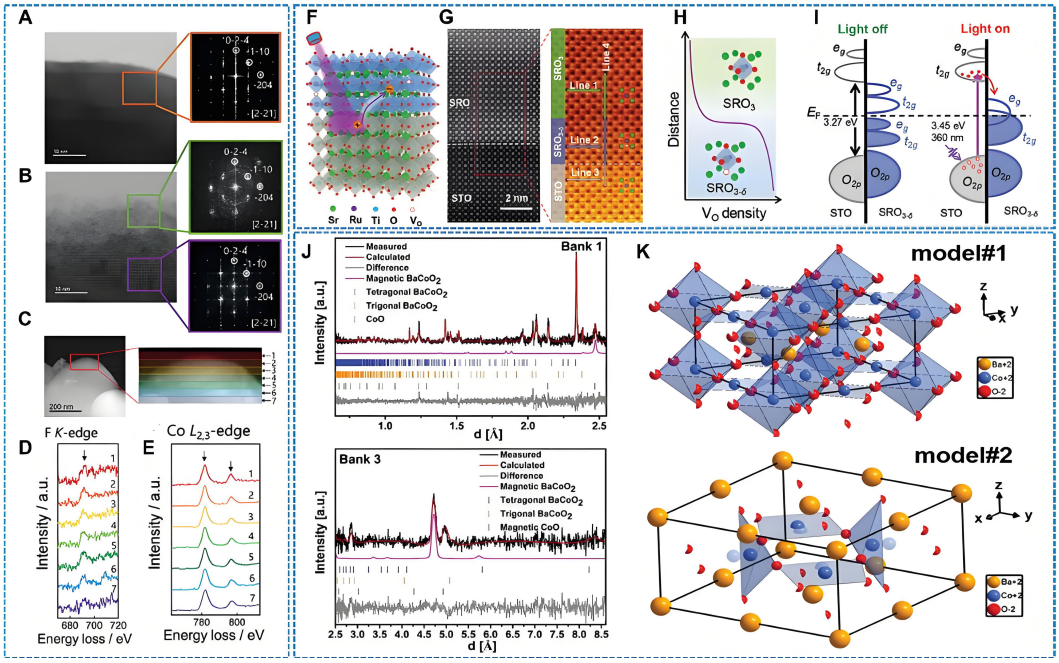

Figure 7. (A) ABF STEM image of pristine LSC55 particles with the FFT pattern of the selected region; (B) ABF STEM image of LSC55-F20 particles with the FFT pattern of the selected region; (C) HAADF image of LSC55-F20 particles; (D) F K-edge spectra. This figure is quoted with permission[80]; (E) Co $L_{2,3}$-edge spectra from the numbered regions in (D); (F) Schematic of photoinduced charge transfer at the SRO/STO interface; (G) High-resolution HAADF-STEM image of the SRO/STO interface with ABF-STEM image of the selected region; (H) Schematic representation of VO distribution in SRO; (I) DOS illustration for the $SRO_{3-\delta}$/STO heterostructure under dark and illuminated conditions. This figure is quoted with permission[81]; (J) Rietveld refinement of X-ray and neutron powder diffraction data; (K) Structural diagram of $BaCoO_{2+\delta}$. This figure is quoted with permission[82]. ABF STEM: Annular bright field scanning transmission electron microscopy; ABF-STEM: annular bright-field scanning transmission electron microscopy; FFT: fast Fourier transform; HAADF-STEM: high-angle annular dark-field scanning transmission electron microscopy; SRO: $SrRuO_3$; STO: $SrTiO_3$; VO: oxygen vacancies; DOS: density of states.

these metastable phases and harnessing their unique properties. The choice of synthesis technique directly influences the resulting crystal structure, defect concentration, and overall stability of the metastable phases. This section delves into the general synthesis methods traditionally applied to metastable materials, their limitations, and how these methods can be adapted or combined to optimize the formation of metastable perovskite oxides. Following this general overview, we will explore specific synthesis strategies tailored to the unique requirements of these oxides.

General synthesis methods and limitations

Synthesizing metastable perovskite oxides using traditional methods is challenging due to their thermodynamic tendency to transition into stable phases. Conventional techniques such as solid-state reactions and sol-gel methods are optimized for stable phases, making it difficult to retain high-energy metastable states. High temperatures and long reaction durations - often exceeding 1,000 °C - promote atomic diffusion, allowing atoms to settle into lower-energy configurations. This is particularly detrimental for metastable phases, as extended high-temperature exposure overcomes kinetic barriers, making it nearly impossible to prevent reversion to the stable phase. Even slight temperature variations can significantly influence metastable phase stability, altering the crystal structure[84].

Conventional methods also rely on slow cooling rates, typically 1 ~ 10 °C min^{-1}, which favor the relaxation of metastable phases into stable forms. In contrast, retaining metastable states often requires rapid quenching at rates of several hundred degrees per minute. Without such fast cooling, metastable structures

gradually revert to stable forms[85]. Additionally, traditional methods operate at ambient pressures, which favor stable phases. In contrast, high-pressure conditions can stabilize metastable configurations, a limitation of conventional synthesis.

Solution-based techniques such as sol-gel and hydrothermal methods, though operating at lower temperatures (usually under 300 °C), also struggle with metastable phase production due to long reaction times and difficulties in controlling nucleation and crystallization. Their slower kinetics often allow stable phases to dominate. For example, the sol-gel process involves slow gelation and crystallization over hours or days, enabling the system to relax into lower-energy configurations. Subsequent calcination (400 ~ 700 °C) further favors stable phase growth, especially with thermal ramp rates below 10 °C min^{-1}[86]. Therefore, final products often contain mixed phases, with metastable forms overshadowed by stable counterparts.

The lack of rapid cooling, high pressure, and precise kinetic control limits the effectiveness of conventional methods in preserving metastable states. For instance, creating oxygen vacancies or defect-rich structures - key features of many metastable perovskite oxides - requires stringent atmospheric control and fast kinetics, which traditional methods cannot provide[87]. Standard oxygen partial pressures (0.1 to 1 atm) are insufficient for maintaining desired defect states or oxidation levels in metastable phases. These limitations underscore the need for advanced synthesis approaches that balance kinetic and thermodynamic factors critical for stabilizing metastable perovskite oxides.

Specific synthesis strategies for metastable perovskite oxides

Specific synthesis methods for metastable perovskite oxides are designed to precisely control the key parameters influencing structural stability and defect concentration. These strategies aim to stabilize high-energy configurations while preventing transitions to stable phases. The following sections provide an in-depth examination of four primary methods tailored to metastable perovskite oxides, focusing on their underlying principles, advantages, and limitations.

Solid-state synthesis

Solid-state synthesis, a common method for fabricating metastable perovskite oxides, requires precise control to avoid transitions to thermodynamically stable phases[88,89]. Unlike conventional solid-state reactions, metastable synthesis demands careful regulation of temperature, atmosphere, and cooling rates. Reaction temperatures are typically lower, ranging from 600 to 900 °C, to limit atomic diffusion and kinetic pathways favoring equilibrium. The exact temperature depends on the composition of perovskite and the target phase, with shorter reaction times employed to reduce prolonged high-temperature exposure. Controlled atmospheres, such as low oxygen partial pressures (e.g., 10^{-4} atm) or reducing gases, are critical for maintaining defect-rich environments and stabilizing metastable phases[90]. This approach is especially important for perovskites with multivalent cations, where oxidation state balance is vital for structural and electronic stability. Oxygen vacancies, managed via tailored atmospheres, enhance electronic conductivity and ionic transport. Precise cooling, often rapid, prevents phase transformations during quenching, while post-synthesis annealing under controlled conditions further tunes defect concentrations without triggering phase transitions. By optimizing these parameters, solid-state synthesis enables the stabilization of metastable perovskite oxides with unique properties for electronic and catalytic applications.

To explore controlled synthesis techniques in achieving metastable perovskite structures, particularly through solid-state processes that allow precise structural modulation, Falmbigl *et al.* synthesized semi-amorphous $Ba(OH)_2$-TiO_2 layered films via atomic layer deposition (ALD) on (100)-oriented silicon substrates and Pt(111)/Ti/SiO_2/Si(100) substrates, achieving a thickness of approximately 50 nm[91]. These

films were annealed at 750 °C to form high-quality polycrystalline $BaTiO_3$. All samples of the metal-insulator-metal (MIM) capacitors were examined through cross-sectional observation to better understand the influence of structure and morphology on physical properties [Figure 8A-D]. Representative bright-field transmission electron microscopy (BF-TEM) images show well-crystallized $BaTiO_3$ films between the electrodes, with grains oriented randomly. FFT analysis of non-overlapping grains identified a random distribution of tetragonal and hexagonal polycrystalline grains, indicating co-crystallization of the two phases during annealing. Building on this, Yamazoe *et al.* studied the synthesis of $KNbO_3$ using a modified solid-state reaction process [Figure 8E][92]. At 480 °C, K_2O reacts with Nb_2O_5 to form metastable $KNbO_3$, which then transitions to a perovskite phase between 480 to 550 °C [Figure 8F]. Urea was found to be critical in facilitating this transformation at lower temperatures (< 500 °C). Usiskin *et al.* synthesized $SrCo_{0.9}Nb_{0.1}O_{3-\delta}$ powder using a conventional solid-state method[93]. Following mixing, grinding, and drying, the material was annealed at 1,200 °C for 10 h. The oxidation range for 3 - δ was found to be between 2.45 and 2.70 across temperatures from 500 to 1,000 °C under oxygen partial pressures ranging from 10^{-4} to 1 bar, indicating both stable and metastable behavior [Figure 8G]. Isotherms based on thermogravimetric analysis showed consistent results for both alternating and stepping sequences at temperatures above 600 °C [Figure 8H].

Exploring further the development of metastable perovskite phases through precision synthesis, Uusi-Esko *et al.* examined the fabrication of hexagonal and orthorhombic $RMnO_3$ thin films. Using advanced ALD followed by nitrogen gas annealing, they employed $R(thd)_3$, $Mn(thd)_3$, and ozone as precursors to control film composition and phase stability[94]. Metastable perovskite formation was enhanced by depositing films on coherent perovskite substrates, resulting in single-phase $RMnO_3$ (R = La to Lu) on LAO. A linear correlation between film thickness and ALD cycle number at 275 °C was established [Figure 8I], demonstrating effective growth control with a constant growth-per-cycle (GPC). Orthorhombic $YbMnO_3$ on STO exhibited minor hexagonal impurities, while the film on LAO maintained single-phase o-$YbMnO_3$. As seen in Figure 8J, hexagonal $YbMnO_3$ was synthesized on silicon at 900 °C but decomposed at 1,000 °C, forming binary oxide impurities, a trend also observed in h-$LuMnO_3$. This work underscores the importance of high-temperature solid-state reactions in synthesizing metastable perovskite oxides. Highlighting the significance of high-temperature solid-state reactions for metastable phase stabilization, Bora *et al.* investigated the phase transformation of $ZnSnO_3$ microcubes (MCs), initially synthesized at room temperature and annealed at 1,000 °C, illustrating the critical influence of temperature in guiding metastable perovskite oxide synthesis[95]. As illustrated in Figure 8K, the transformation begins with the dissolution of the metastable $ZnSnO_3$ phase at approximately 200 °C, leading to an amorphous state lacking Raman-active bands. At around 500 °C, phase transformation proceeds through redeposition, a process known as Ostwald ripening. Finally, at 750 °C, the sample recrystallizes into the stable inverse spinel Zn_2SnO_4, with SnO_2 formation.

High-pressure synthesis

High-pressure synthesis effectively stabilizes metastable perovskite oxides that cannot form under ambient conditions by shifting the thermodynamic equilibrium, enabling the formation of high-energy phases that would typically revert to stable forms at standard pressure[96]. Applying pressures of several to tens of gigapascals (GPa) alters the energy landscape, reducing unit cell volume and stabilizing phases with unusual cation coordination and distorted octahedral geometries. For instance, high pressure changes octahedral tilting angles, modifying the band structure of material, ionic conductivity, and defect concentration. This method allows precise control over lattice parameters, compressing constants by several percent to create denser atomic packing, which enhances properties such as charge carrier mobility and ionic conductivity, crucial for optoelectronics and energy devices[97].

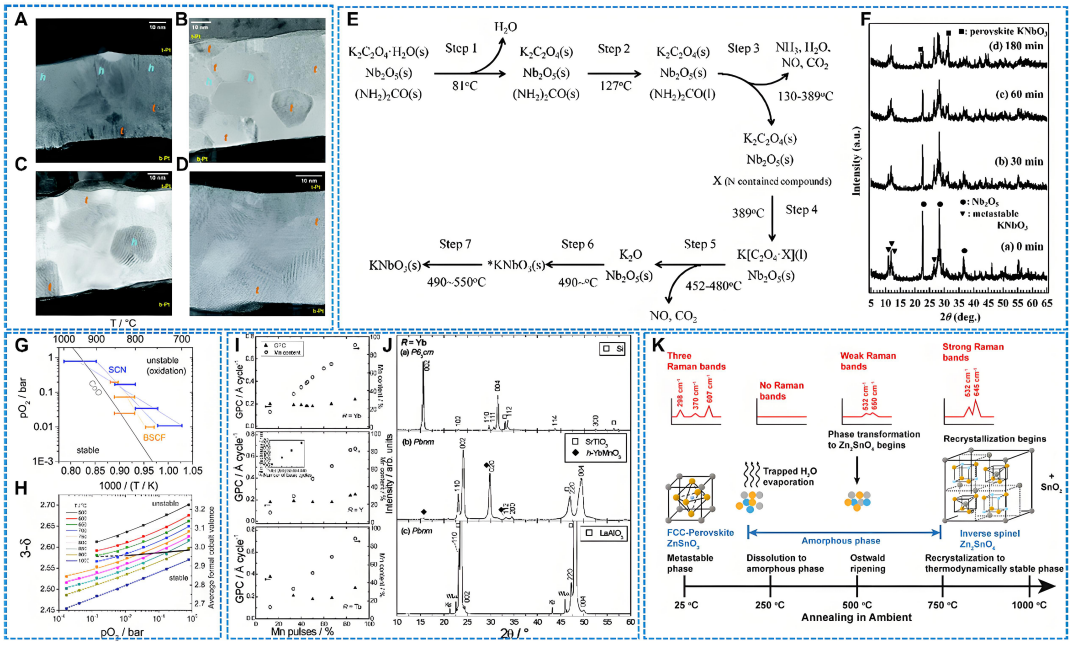

Figure 8. BF-TEM cross-sectional images of MIM capacitors annealed at 750 °C, with Ba/Ti ratios of (A) 0.80; (B) 0.92; (C) 1.01; and (D) 1.06. This figure is quoted with permission[91]; (E) schematic diagram of the $KNbO_3$ synthesis mechanism via a modified solid-state reaction method; (F) HT-XRD patterns of a 1:1:1 mixture of $K_2C_2O_4{\cdot}H_2O$, Nb_2O_5, and urea. This figure is quoted with permission[92]; (G) Stability limit of $SrCo_{0.9}Nb_{0.1}O_{3-\delta}$; (H) Oxidation stoichiometry of $SrCo_{0.9}Nb_{0.1}O_{3-\delta}$. This figure is quoted with permission[93]; (I) Correlation between precursor pulse ratio and actual Mn content in $RxMnyO_3$ thin films, along with the linear relationship between film thickness and ALD cycle number for $YxMnyO_3$ films; (J) XRD patterns of $YbMnO_3$ thin films. This figure is quoted with permission[94]; (K) schematic representation of the phase transformation process of $ZnSnO_3$ during annealing. This figure is quoted with permission[95]. BF-TEM: Bright-field transmission electron microscopy; MIM: metal-insulator-metal; HT-XRD: high-temperature X-ray diffraction; ALD: atomic layer deposition; XRD: X-ray diffraction.

High pressure also facilitates higher concentrations of oxygen vacancies (10^{18} to 10^{21} cm^{-3}), improving ion transport and altering electronic environments, making these materials suitable for solid oxide fuel cells and oxygen separation membranes. Extreme pressure can support multiple oxidation states, enabling redox reactions. However, careful pressure release is required to prevent phase reversion, as rapid decompression may cause structural collapse or phase transitions. Scalability is also challenging due to the cost and complexity of equipment for pressures above 10 GPa. Despite these limitations, high-pressure synthesis offers a unique approach to tuning structural and electronic properties beyond conventional techniques.

Building on the potential of high-pressure techniques to stabilize unique perovskite phases, Ishiwata *et al.* synthesized single-crystal orthorhombic $YMnO_3$ (o-$YMnO_3$) using a quasi-hydrothermal approach under 5.5 GPa. Black crystals (0.5 mm × 0.4 mm × 0.4 mm) were obtained [Figure 9A][98]. Laue XRD revealed the crystal orientation, with the shiny facet corresponding to the c-plane in the Pbnm setting. The lattice parameters of single-crystal o-$YMnO_3$ were [a = 5.261(3) Å, b = 5.843(4) Å, c = 7.356(5) Å], closely matching those of polycrystalline o-$YMnO_3$. These results confirm the stabilization of the metastable orthorhombic phase under high pressure at ambient conditions. Magnetic measurements show that o-$YMnO_3$ exhibits a stable E-type antiferromagnetic ground state. A spiral spin phase forms at intermediate temperatures, enhancing its electromagnetic response. As shown in Figure 9B, o-$YMnO_3$ demonstrates significant magnetocapacitance and magnetoelectric effects. Spin alignment along the b-axis contributes to spontaneous polarization along the a-axis, highlighting its potential for multiferroic applications. Inaguma *et al.* synthesized polar lithium niobate-type (LN-type) $ZnTiO_3$ under high-pressure and high-temperature conditions, starting from ilmenite-type (IL-type)[99]. First-principles calculations indicated that LN-type

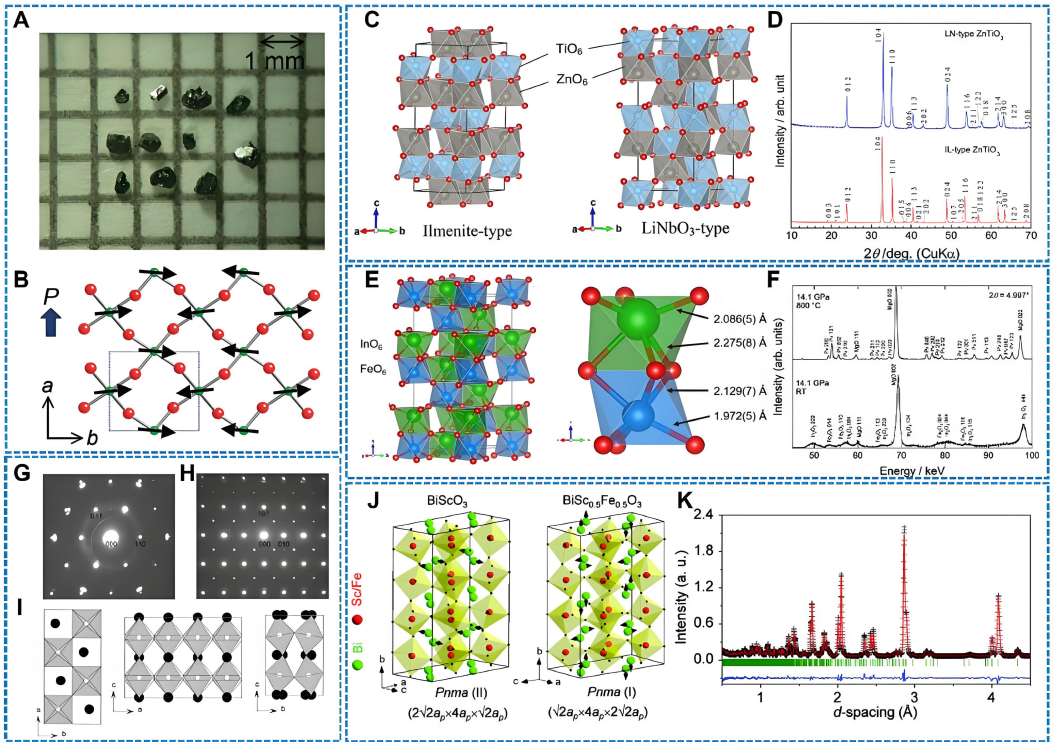

Figure 9. (A) Single-crystal perovskite-type $YMnO_3$; (B) Schematic representation of the E-type antiferromagnetic ordering structure of the MnO_2 plane. This figure is quoted with permission[98]; (C) Structural diagram of ilmenite-type and $LiNbO_3$-type $ZnTiO_3$; (D) XRD patterns of LN-type and IL-type $ZnTiO_3$. This figure is quoted with permission[99]; (E) Polyhedral representation of the $LiNbO_3$-type $InFeO_3$ crystal structure refined using TOF NPD data, showing the local coordination environment of the stacked InO_6 and FeO_6 octahedra; (F) *In situ* SXRD pattern of $InFeO_3$. This figure is quoted with permission[100]; (G) and (G) Electron diffraction patterns of BMT; (I) Polyhedral representation of the crystal structure corresponding to the Pbam space group. This figure is quoted with permission[101]; (J) Schematic diagrams of the two Pnma structures; (K) Rietveld refinement of the neutron diffraction pattern. This figure is quoted with permission[102]. XRD: X-ray diffraction; LN-type: lithium niobate-type; IL-type: ilmenite-type; TOF: time-of-flight; NPD: SXRD: synchrotron X-ray diffraction; BMT: $Bi(Mg_{0.5}Ti_{0.5})O_3$.

$ZnTiO_3$ is a metastable phase formed through decompression of the stable perovskite phase. The connectivity of BO_6 octahedra differs between IL-type and LN-type $ZnTiO_3$: in the IL-type, AO_6 and BO_6 octahedra are edge-sharing, while in the LN-type, they are corner-sharing [Figure 9C]. The powder XRD pattern [Figure 9D] confirmed phase transformation. Additionally, the positive SHG response indicates a non-centrosymmetric structure. High-pressure synthesis of LN-type $ZnTiO_3$ suggests its potential for epitaxial stabilization in thin-film applications. Fujita *et al.* proposed synthesizing polar magnets within $AFeO_3$ perovskites using small A-site cations with low tolerance factors[100]. $InFeO_3$, adopting a $LiNbO_3$-type structure (R3c space group) [Figure 9E], was confirmed as a room-temperature polar magnet. This metastable compound, originating from an orthorhombic perovskite phase (Pnma or Pn21a), is stabilized under high-pressure (15 GPa) and elevated temperatures [Figure 9F], opening the door for room-temperature magnetoelectric coupling.

Despite challenges in synthesizing certain perovskite phases at ambient pressure, high-pressure techniques techniques effectively stabilize these metastable configurations. Khalyavin *et al.* successfully synthesized the metastable $Bi(Mg_{0.5}Ti_{0.5})O_3$ (BMT) perovskite phase under 6 GPa and 1,270 K, a phase inaccessible by conventional methods[101]. As illustrated in Figure 9G and H, they observed the absence of specific superstructure reflections in certain $<111>_p$ patterns, indicating the exclusion of in-phase octahedral tilting. Conversely, reflections of antiphase octahedral tilting observed in $<110>_p$ patterns aligned with XRD data.

X-ray and electron diffraction revealed complex superstructure of BMT, resulting from displacement of Bi^{3+} cations and octahedral tilting. Theoretical analysis confirmed two possible crystal structures: $a^+b^0_0a^-$ (space group Pbam) [Figure 9I] and $a^+b^0_0a^+$ (space group Pnnm), clarifying octahedral tilting within the orthorhombic unit cell. Notably, many phases can be stabilized under high-pressure and high-temperature conditions and then quenched to ambient conditions, where they retain dynamic stability and exhibit distinctive properties. Khalyavin *et al.* used high-pressure synthesis to fabricate metastable $BiFe_{1-y}ScyO_3$ perovskite, revealing irreversible phase transitions during annealing, termed "transition polymorphisms"[102]. These transitions lead to diverse polycrystalline structures at ambient conditions, demonstrating unique magnetic properties. While observed in other systems, they are particularly remarkable across the $BiFe_{1-y}Sc_yO_3$ series. Atomic coordinates of $BiScO_3$ were determined through combined X-ray and neutron diffraction, supported by DFT calculations [Figure 9J]. As shown in Figure 9K, the primary structural distortions include reverse octahedral tilting and antiferroelectric-like cation displacements, with cation displacements being the key driver of superstructure formation.

Pulsed laser deposition

PLD is an effective method for synthesizing metastable perovskite oxides, offering precise control over film composition, crystallinity, and quenching rates. High-energy laser pulses vaporize a target, creating a plume that condenses onto a substrate[103,104]. Rapid quenching prevents phase transitions into stable configurations, ideal for trapping metastable phases. Unlike bulk methods, PLD enables atomic-level control over layer thickness and composition, facilitating heterostructures and superlattices with tunable interfacial properties. The dynamic deposition atmosphere allows precise control over oxygen vacancies and cation oxidation states, optimizing ionic and electronic transport properties. Adjusting oxygen partial pressures during deposition tailors bandgap energies, crucial for metastable perovskite performance[11]. In-situ annealing enhances crystallinity and refines defect concentrations without inducing phase transitions. However, parameters such as laser fluence, target-substrate distance, and substrate temperature must be carefully optimized to avoid stable phase formation. While precise, PLD faces challenges in scalability and cost for large-scale production[105].

The commercialization of palladium-based catalysts (PPC) is limited by their susceptibility to poisoning, recovery challenges, and loss of catalytic activity. Wu *et al.* deposited palladium nanoparticles (NPs) on amorphous SRO thin films using PLD on glassy carbon electrodes (GC), followed by deposition of Pd NPs under vacuum (10^{-4} Pa) at room temperature [Figure 10A and B][106]. HRTEM revealed crystalline (110) Pd NPs (~ 2 nm) embedded in the SRO matrix. The Pd/a-$SrRuO_3$/GC hybrid catalyst exhibited superior electrocatalytic oxidation reaction (EOR) activity of 4.0 A mg^{-1} Pd and excellent durability, retaining 3.0 A mg^{-1} Pd after 1,000 cycles, with a self-adapting region beyond 400 cycles. The catalyst also demonstrated a high mass activity of 0.57 A mg^{-1} Pd after 60,000 s of continuous operation. Remarkably, after five CV cycles in 1 M KOH, recovery efficiency reached ~ 98%, ten times higher than commercial Pd/C (~ 9.2%). These results highlight the self-cleaning, self-adapting, and reactivation properties of Pd/a-$SrRuO_3$/GC catalysts, offering a promising solution for durable EOR catalysts in direct ethanol fuel cell (DEFC) applications. Schraknepper *et al.* investigated the deposition of SRO thin films on (100)-oriented, undoped SRO substrates using PLD[107]. Oxygen vacancy behavior was examined through $^{16}O/^{18}O$ exchange anneals. The PLD-grown films exhibit a metastable point-defect structure that may relax to equilibrium under sufficient time or temperature. As shown in Figure 10C, atomic force microscopy reveals a terrace structure mimicking the underlying SRO substrate, with occasional screw-like formations from threading dislocations. Reciprocal space mapping confirmed that the in-plane lattice parameter of SRO matches the substrate, confirming epitaxial growth and high crystalline quality. The observed low oxygen tracer diffusion coefficient (D^*_o) [Figure 10D] and low oxygen vacancy fraction (n_v) are likely due to the distinctive

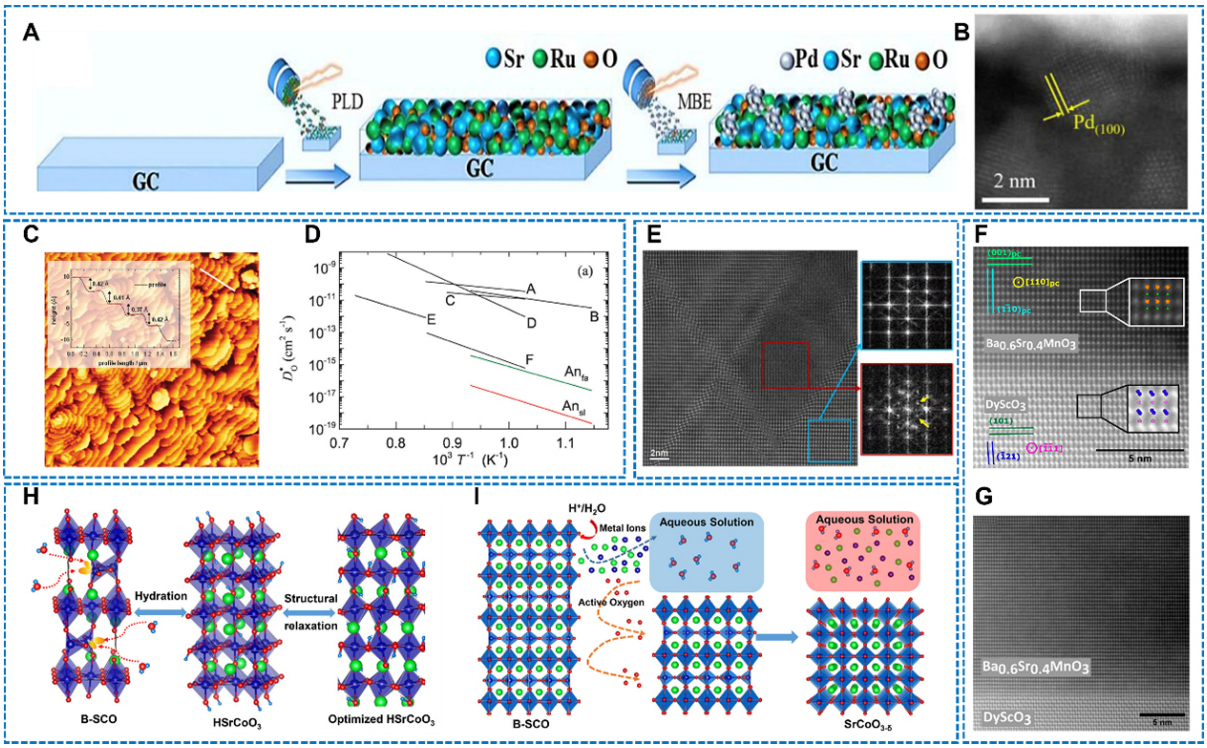

Figure 10. (A) Schematic illustration of the preparation process of Pd/a-$SrRuO_3$ hybrid films by PLD; (B) HRTEM planar view of the Pd/a-$SrRuO_3$ sample. This figure is quoted with permission[106]; (C) Atomic force microscopy image of the surface morphology of the $SrRuO_3$ thin film; (D) Oxygen tracer diffusion coefficient. This figure is quoted with permission[107]; (E) Cross-sectional HAADF-STEM image of $(Sr_{0.6}Ba_{0.4})MnO_3$ thin film, with FFT highlights of the perovskite and hexagonal phases. This figure is quoted with permission[108]; (F) High-magnification cross-sectional HAADF-STEM image of $Ba_{0.6}Sr_{0.4}MnO_3$ thin film; (G) Low-magnification cross-sectional HAADF-STEM image of $Ba_{0.6}Sr_{0.4}MnO_3$ thin film. This figure is quoted with permission[109]; (H) Mechanism A: Conversion of B-SCO to $HSrCoO_3$ through a quasi-nucleophilic addition process; (I) Mechanism B: Oxidation of the underlying B-SCO by active oxygen. This figure is quoted with permission[110]. PLD: Pulsed laser deposition; HRTEM: high-resolution transmission electron microscopy; HAADF-STEM: high-angle annular dark-field scanning transmission electron microscopy; FFT: fast Fourier transform; B-SCO: brownmillerite $SrCoO_{2.5}$.

defect chemistry of SRO and the metastable nature of PLD-produced films.

A novel FE mechanism, driven by off-centering magnetic Mn^{4+} ions in $(Sr_{1-x}Ba_x)MnO_3$, particularly in its ideal perovskite phase, presents considerable promise for advancing strong magnetoelectric materials. However, stabilizing this phase in thin films remains challenging due to its metastability. Langenberg *et al.* investigated the stabilization of the perovskite phase in $(Sr_{1-x}Ba_x)MnO_3$ thin films synthesized via PLD on (001)-oriented perovskite substrates[108]. FFT analysis of regions between twin domains revealed the coexistence of the desired perovskite phase and a competing hexagonal phase [Figure 10E], underscoring the complexity of phase competition. This study demonstrates the utility of PLD techniques in stabilizing metastable perovskite oxides and their potential for novel magnetoelectric applications. Zhou *et al.* successfully stabilized the 3C phase of $Ba_{0.6}Sr_{0.4}MnO_3$ using regular PLD (rPLD) on $DyScO_3$ (101)o substrates with a 0.1% O_2 and 99.9% N_2 gas mixture[109]. To further improve stability, intermittent PLD (iPLD) was employed, providing enhanced kinetic control by incorporating relaxation intervals between pulses. This approach facilitated layer-by-layer (LBL) growth, achieving a single-phase 3C structure with a film thickness of approximately 40 nm. The epitaxial (001)pc $Ba_xSr_{1-x}MnO_3$ (BSMO) film exhibited coherent alignment with the $DyScO_3$ substrate, confirming high crystalline quality [Figure 10F]. Furthermore, a lower magnification image from a different region [Figure 10G] showed a defect-free film over a larger area,

despite a 1.80% lattice mismatch, indicating structural integrity under strain. These results suggest that iPLD enhances nucleation and facilitates the epitaxial stabilization of higher Ba-content BSMO within the 3C structure. Overall, this study demonstrates iPLD's potential to overcome rPLD's kinetic constraints, enabling the production of thicker, single-phase metastable perovskite oxides with improved stability. In a recent study, Wang *et al.* proposed a detailed interaction mechanism between brownmillerite $SrCoO_{2.5}$ (B-SCO) thin films and the metastable perovskite phase (M-SCO)[110]. Epitaxial B-SCO films were synthesized using a PLD system to examine this interaction. Mechanism A describes the formation of M-SCO ($HSrCoO_3$) as a hydrated derivative of B-SCO [Figure 10H]. Mechanism B suggests that protons dissolve the B-SCO surface, releasing Sr^{2+}, Co^{2+} and oxygen species, which either form O_2 molecules or migrate to the B-SCO to occupy vacancies [Figure 10I]. This results in the formation of $SrCoO_{3-\delta}$, with a high density of oxygen vacancies, enhancing the metastable characteristics of M-SCO.

Other approaches

Salt-assisted and wet chemical methods offer distinct advantages for synthesizing metastable perovskite oxides by controlling phase formation, defect incorporation, and material properties[111]. Salt-assisted synthesis uses molten salts to enhance ion mobility and accelerate nucleation, enabling crystal growth at lower temperatures (500 to 700 °C), while stabilizing high-energy metastable phases[112]. The molten salt reduces diffusion barriers, promotes uniform crystal growth, and prevents stable phase formation. It also influences product morphology, often favoring anisotropic growth, which enhances properties such as ion transport and electronic conductivity. Additionally, this method precisely controls oxygen vacancies and cation coordination, critical for metastable configurations. Wet chemical methods, operating at lower temperatures, achieve fine control over precursor chemistry and reaction kinetics[113]. Aqueous or organic solvents provide a homogeneous medium, allowing precise control of parameters such as pH, solvent composition, and precursor concentrations. These factors stabilize metastable phases and desired defect states, such as oxygen vacancies, which improve ion transport and catalytic activity[114]. The low-temperature synthesis and controlled kinetics ensure metastable structures remain intact while enabling property tuning for applications requiring high ionic conductivity and tailored electronic structures.

A promising yet underexplored approach is flash Joule heating (FJH), which has potential for fabricating high-entropy and metastable materials. Its rapid, localized heating can stabilize metastable phases, providing a scalable route for synthesizing perovskite oxides with tailored properties. Though its use in perovskite oxides remains limited, combining FJH with other techniques could expand opportunities for metastability optimization.

Under conventional conditions, $ReNiO_3$ exhibits a positive Gibbs free energy (ΔG), limiting its synthesis through traditional methods. Nevertheless, Yan *et al.* successfully synthesized $ReNiO_3$ films (Re = Sm, Nd, Eu, and Gd) on LAO (001) and STO (001) substrates using a wet chemical method involving spin coating, followed by annealing at 800 °C under 1 atm and 15 MPa oxygen pressure[115]. Calculations of interface-free energies [Figure 11A] showed negative values, indicating that interfacial conditions reduce $ReNiO_3$'s positive Gibbs energy, promoting nucleation on LAO and STO substrates. Moreover, $ReNiO_3$ films grown on LAO single-crystal substrates [Figure 11B] crystallized effectively at atmospheric pressure, eliminating the need for elevated oxygen pressures. This suggests that interface bonding with the substrate lowers the positive Gibbs formation energy of $ReNiO_3$, supported by first-principles calculations.

In addition to wet chemical synthesis methods, salt-assisted techniques have proven effective for synthesizing metastable perovskite oxides. Li *et al.* synthesize $RENiO_3$ in quantities up to 20 g per batch via a KCl-assisted molten salt reaction [Figure 11C], advancing its potential for device applications while

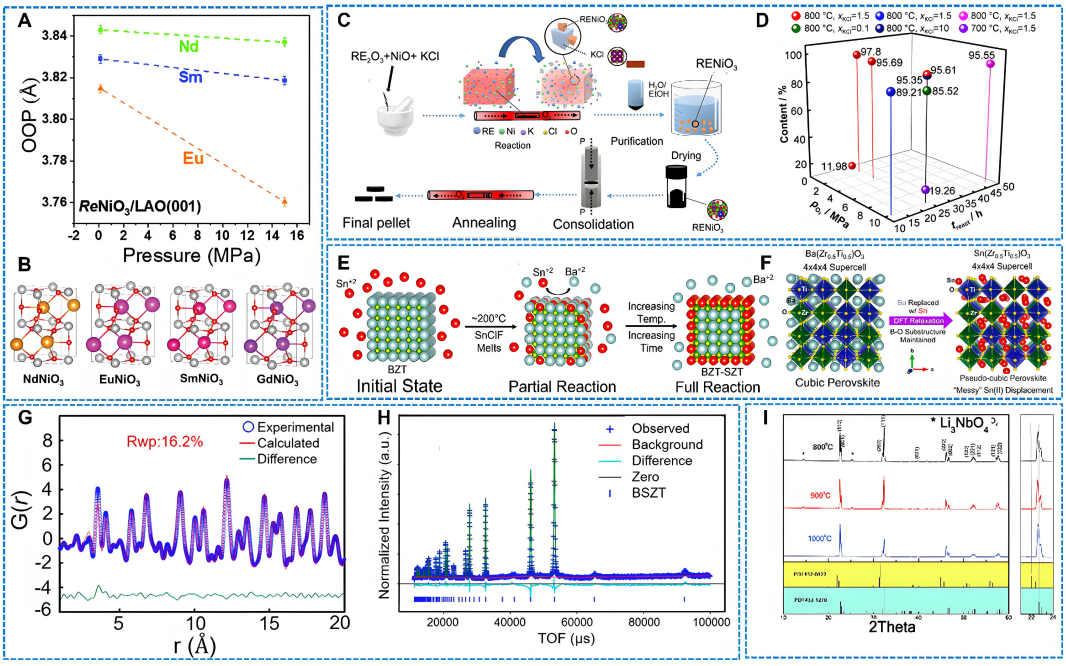

Figure 11. (A) Out-of-plane lattice constant calculations for $ReNiO_3$/LAO (001) (Re = Sm, Nd, and Eu) films; (B) Unit cell structures of $SmNiO_3$, $NdNiO_3$, $EuNiO_3$, and $GdNiO_3$. This figure is quoted with permission[115]; (C) Schematic flowchart for the molten salt-assisted synthesis of $RENiO_3$; (D) Content of $SmNiO_3$ in samples prepared under different conditions. This figure is quoted with permission[116]; (E) Schematic illustration of Sn(II) exchange on the surface of BZT particles; (F) Rietveld refinement of XRD data. This figure is quoted with permission[117]; (G) Rietveld refinement of room-temperature neutron diffraction data; (H) Refinement of the pair distribution function using a cubic perovskite model. This figure is quoted with permission[68]; (I) XRD pattern of KNLN microcrystals. This figure is quoted with permission[118].BZT: $Ba(Zr_{0.5}Ti_{0.5})O_3$; XRD: X-ray diffraction; KNLN:$(K_{0.5}Na_{0.5})_{0.95}Li_{0.05}NbO_3$.

lowering production costs[116]. The resulting powders exhibited a cubic morphology with an average particle size of approximately 2 μm and phase purity greater than 95%. Figure 11D shows the $SmNiO_3$ content under different preparation conditions. Optimization synthesis parameters revealed that maintaining the reaction temperature above KCl's melting point is key for promoting nucleation of the metastable $RENiO_3$ phase. Furthermore, an oxygen pressure of 1.5 MPa suffices for high phase purity, and using rare earth extraction intermediates further reduces costs.

Furthermore, Li *et al.* present the first synthesis of a Sn(II) perovskite oxide, $Sn(Zr_{0.5}Ti_{0.5})O_3$ (SZT), as a nanoshell around a SZT core[117]. The metastable SZT dielectric was produced via a low-temperature flux reaction using a NaCl-KCl eutectic mixture and low-melting SnClF. This methodology effectively reduces temperature and mitigates cation diffusion during exchange, improving kinetic stability. As shown in Figure 11E, the reaction begins at 200 °C, where $SnCl_2/SnF_2$ melts and coats the $Ba(Zr_{0.5}Ti_{0.5})O_3$ BZT particles. The exothermic formation of BaClF from SnClF (-1,028 kJ mol^{-1}) drives the exchange. At elevated temperatures, Sn(II) cations diffuse into the BZT particles and exchange with Ba(II) cations. Geometry relaxations of the cubic SZT structure, analyzed via DFT, reveal random distortions of the Sn(II) cations [Figure 11F]. Using the same preparation method, O'Donnell *et al.* employed low-temperature salt flux reactions to facilitate destabilizing Sn(II) cation in $BaZrO_3$, $BaTiO_3$, and $Ba(Zr_{1-y}Ti_y)O_3$ solid solutions, resulting in highly metastable compositions[68]. The synthesis yielded bulk perovskites containing the highest known concentrations of Sn(II) cations, extending the boundaries of metastability. Comprehensive showed that the compounds possess cubic perovskite structures, becoming more metastable with higher Sn(II) and Zr(IV) concentrations. The kinetic stability is attributed to the cohesive energy of the perovskite framework and its resulting limitation of ion diffusion. Rietveld refinements of $(Ba_{1-x}Sn_x)(Zr_{0.5}Ti_{0.5})O_3$ confirmed a cubic

structure with weighted residuals of approximately 3%-6% [Figure 11G]. These results, along with reduced unit cell dimensions [Figure 11H], suggest that low-temperature salt flux reactions are an effective strategy for synthesis of highly metastable perovskites. Due to the typically multi-step nature of molten salt synthesis, Liu *et al.* focused on synthesizing and investigating the phase transition characteristics of metastable perovskite oxides, specifically $K_{0.5}Na_{0.5}NbO_3$ and $K_{0.4}Na_{0.4}Li_{0.2}NbO_3$, using a combination of solid-phase reactions and molten salt methods[118]. The introduction of Li^+ was found to inhibit the transformation from perovskite to tungsten bronze. Figure 11I shows that calcination at 800 °C produced a perovskite phase with trace Li_3NbO_4 impurities. At 900 °C, the second phase diminished, and pure $K_{0.5}Na_{0.5}NbO_3$ was obtained at 1,000 °C. The phase transition from cubic (C) to tetragonal (T) was characterized by three specific temperatures, with the Curie temperature (Tc) marking the equilibrium between the T and C phases. Within the temperature range of 400 °C to Tc, the metastable T phase persisted, indicating that the crystalline structure of microcrystals synthesized at 1,000 °C is the most stable configuration.

Summary of reported metastable perovskite oxides

The compilation of studies on metastable perovskite oxides, as outlined in Table 1, reveals critical insights into the interplay between synthesis techniques, structural modifications, and resultant functional enhancements across various applications. Metastable perovskite oxides are primarily synthesized through high-precision methods, such as solid-state reactions in controlled atmospheres, high-pressure synthesis, PLD, and salt-assisted approaches[119]. These methods are instrumental in achieving the kinetic stabilization necessary to retain metastable phases, particularly by introducing structural features such as oxygen vacancies, octahedral distortions, and lattice strain. Such structural attributes not only preserve the high-energy states but also drive desirable electronic and ionic properties. The selective control over oxygen vacancy concentrations and cation oxidation states is particularly impactful, as it influences charge distribution, electronic conductivity, and ionic mobility, all essential for their performance across applications in catalysis, energy storage, and electronic devices.

In electromagnetic and dielectric applications, metastable perovskite oxides demonstrate tunable dielectric constants and insulating capabilities, which are highly advantageous for capacitors and high-frequency devices[120]. By carefully modulating oxygen vacancies and the oxidation states of cations, these materials achieve enhanced dielectric properties, allowing precise control over insulating performance - a critical feature for miniaturized and high-performance electronic components. Furthermore, structural tuning through oxygen vacancy control has been shown to directly affect emission properties in light-emitting diode (LED) applications, where optimized vacancy concentrations contribute to higher emission efficiency and improved color purity, making these oxides attractive candidates for advanced optoelectronic devices[121]. Metastable perovskite oxides are also highly effective in FE and piezoelectric devices, where their unique structural flexibility enables enhanced piezoelectric responses suitable for sensors, actuators, and energy-harvesting systems[122]. The ability to stabilize specific metastable phases significantly amplifies their piezoelectric and FE behavior, and the incorporation of multivalent cations and oxygen vacancies further elevates their performance in non-volatile memory devices and next-generation electronic applications. These features underscore the potential of metastable perovskites to serve as critical materials in memory storage technologies, where high retention, low power consumption, and efficient data storage are paramount[123]. In catalysis, metastable perovskite oxides demonstrate remarkable efficacy in photocatalytic applications, such as water splitting and CO_2 reduction[89]. Their structural distortions enhance light absorption and facilitate electron transfer, crucial for maximizing reaction efficiency. The intrinsic flexibility in their lattice structure aids ion transport, improving charge/discharge rates and cycling stability - qualities that are essential for energy storage applications, including supercapacitors and solid-state batteries[35,124]. The stabilization of multiple oxidation states within the lattice also enhances catalytic and electrochemical stability of these materials, supporting prolonged operational performance under challenging conditions.

Table 1. Summary of reported metastable perovskite oxides synthesis and applications

Materials	Fabrication	Temperature	Pressure	Applications	Ref.
$SrTiO_3$	-	-	-	Energy storage	[59,60]
$CaTiO_3$	PLD	600 °C	10 mTorr	Dielectric	[61]
$ScFeO_3$	Solid-state synthesis	1400 °C	ambient pressure	Electromagnetic	[62]
$SnHfO_3$	Solid-state synthesis	300 °C	-	Piezoceramic	[64]
Li_2TiTeO_6	Solid-state synthesis	600 °C	-	Electromagnetic	[65]
Li_2TiTeO_6	Solid-state synthesis	600 °C	-	Electromagnetic	[66]
$SrRuO_3$	PLD	680 °C	100 mTorr	-	[70]
$SrTiO_3/SrIrO_3$	PLD	550 °C	10^{-1} mbar	-	[71]
$SrRuO_3$	PLD	750 °C	-	Energy storage	[72]
$ALa_{1-x}Ta_2O_7:xBi^{3+}$ (A = K and Na)	Salt-assisted	400 °C or 350 °C	-	LED device	[76]
$Dy_2Ti_2O_7$	Solid-state synthesis	1,200 °C	-	Nanocomposite	[77]
$Ln_2Ti_2O_7$	Sol-gel route	-	-	Ferroelectric/ Piezoelectric	[78]
$Sm_2Ti_2O_7$	Sol-gel route	-	-	Photocatalyst	[79]
$La_{0.5}Sr_{0.5}CoO_{3-\delta}$	Anion doping	250 °C	-	Energy storage	[80]
$SrRuO_{3-}$	PLD	-	-	Light-controlled device	[81]
$BaCoO_{2+\delta}$	Solid-state synthesis	-	-	-	[82]
$BaTiO_3$	Solid-state synthesis	750 °C	-	-	[91]
$KNbO_3$	Solid-state synthesis	800 °C	-	-	[92]
$SrCo_{0.9}Nb_{0.1}O_{3-\delta}$	Solid-state synthesis	1,200 °C	-	Catalysts	[93]
$RMnO_3$ (R = Y, La, Sm, Tb, Yb, Lu)	Solid-state synthesis	600-1,000 °C	-	-	[94]
$YMnO_3$		1,280-1,100 °C	5.5 GPa	Energy storage	[98]
$ZnTiO_3$	High-pressure synthesis	1,100-1,200 °C	16-17 GPa	Ferroelectric	[99]
$InFeO_3$	High-pressure synthesis	1,450 °C	5 GPa	Ferroelectric	[100]
$Bi(Mg_{1/2}Ti_{1/2})O_3$	High-pressure synthesis	1,270 K	6 GPa	-	[101]
$BiFe_{1-y}Sc_yO_3$	High-pressure synthesis	-	-	-	[102]
$Pd/a\text{-}SrRuO_3$	PLD	-	104 Pa	Catalysts	[106]
$SrRuO_3$	PLD	973 K	-	Electrode	[107]
$(Sr_{1-x}Ba_x)MnO_3$	PLD	700-1,000 °C	10^{-5} Torr and 10^{-1} Torr	Electromagnetic	[108]
$Ba_{0.6}Sr_{0.4}MnO_3$	PLD	900 °C	2 mTorr	-	[109]
$ReNiO_3$	Wet chemical method	-	-	-	[115]
$RENiO_3$	Salt-assisted method	800-900 °C	8-10 MPa	Energy storage	[116]
$Sn(Zr_{1/2}Ti_{1/2})O_3$	Salt-assisted method	1,100 °C	-	Dielectric semiconductors	[117]
$(Ba_{1-x}Sn_x)(Zr_{1-y}Ti_y)O_3$	Salt-assisted method	1,100 °C	-	Photocatalytic	[68]
$(K, Na)NbO_3$	Salt-assisted method	800 °C	-	Energy storage	[118]

PLD: Pulsed laser deposition; LED: light-emitting diode.

All in all, the unique structural attributes of metastable perovskite oxides, in conjunction with specialized synthesis techniques, endow these materials with versatile properties that are advantageous across a wide range of fields, from high-frequency electronics to sustainable energy solutions. Continued advancements in synthesis methods and a deeper understanding of structure-property relationships will undoubtedly expand the functional potential of metastable perovskite oxides, establishing them as cornerstone materials in emerging energy and information technologies.

CONCLUSION AND FUTURE PERSPECTIVES

This review delivers a thorough examination of metastable perovskite oxides, emphasizing their structural adaptability, defect modulation, and the resultant effects on their physicochemical attributes. By exploring the complex interplay between structure and synthesis, it illuminates how meticulously tailored metastable configurations can lead to novel functionalities. The categorization of metastable perovskites into four primary structural types provides a fresh perspective on how deviations from ideal symmetry, heterojunction formation, layered architectures, and multivalent mechanisms distinctly enhance these materials' performance in key applications. Additionally, our analysis of specific synthesis methodologies highlights the critical need for customized approaches to stabilize these nonequilibrium phases. This review thus emphasizes the essential role of metastable oxides in propelling advancements in next-generation functional materials, underscoring the interdependence of synthesis, structure, and performance.

Metastable perovskite oxides hold transformative potential, but their integration into advanced materials faces significant challenges. Addressing these requires both technical innovation and a deeper understanding of the intrinsic limitations of metastable phases:

(1) Dynamic phase instability: Metastable phases naturally revert to thermodynamically stable forms, particularly under high temperatures or reactive environments, complicating synthesis and long-term stability. Achieving and sustaining these high-energy configurations necessitates techniques that kinetically stabilize metastable states while preserving functionality. Strategies include atomic-level manipulation of energy barriers and advanced in-situ monitoring to enable precise control of phase stability.

(2) Kinetic control in synthesis: Current synthesis methods often lack the precision to consistently produce metastable perovskites at scale. Challenges lie in managing diffusion rates, reaction timing, and thermal profiles. Enhancing localized control over nucleation and diffusion while ensuring scalability is critical. Innovative platforms combining extreme conditions (e.g., high pressure and rapid cooling) with real-time feedback offer promising solutions for dynamic parameter adjustment during synthesis.

(3) Complex defect engineering: The properties of metastable perovskites depend on precise defect configurations, such as oxygen vacancies and cation ordering. Achieving controlled, reproducible defect modulation to enhance ionic conductivity or catalytic activity without compromising structural integrity remains challenging. Advanced synthetic methods, informed by computational models predicting defect formation energies, are needed to optimize defect densities. Additionally, understanding defect dynamics under operational stress requires high-resolution tools for atomic-scale monitoring.

(4) Scalability and environmental impact of synthesis methods: While advanced synthesis methods show promise at the laboratory scale, scaling these techniques for large-scale production remains a challenge. The development of energy-efficient, cost-effective, and reproducible synthesis methods is essential to making metastable perovskite oxides commercially viable. Additionally, the environmental impact of these synthesis processes must be carefully evaluated, focusing on minimizing waste, reducing energy consumption, and using sustainable materials, which will be essential for their industrial application.

Metastable perovskite oxide research is poised to advance through the integration of cutting-edge synthesis techniques, theoretical modeling, and high-throughput experimentation. Innovative methods such as pressure-assisted rapid quenching and controlled reactive atmospheres are critical for scaling the stabilization of metastable phases. In-situ characterization techniques enabling real-time observation of phase formation and stability during synthesis will provide valuable insights, enhancing control over

metastability. Additionally, the application of machine learning and computational materials science will accelerate the discovery of new metastable phases by predicting optimal synthesis conditions and identifying favorable structural configurations. These materials hold great promise for energy storage, catalysis, and optoelectronics, where their tunable electronic properties and defect-rich environments could drive transformative advancements. As efforts converge to bridge the gap between synthesis and functionality, metastable oxides are expected to spearhead the development of high-performance materials, setting new benchmarks for efficiency, stability, and adaptability in advanced technologies.

DECLARATIONS

Authors' contributions

Feng Y, Dai J, and Wang M contributed equally to this work.
Conceptualization: Wan, J.; Feng, Y.; Dai, J.
Formal analysis: Feng, Y.; Dai, J.; Wang, M.
Software: Dai, J.; Wang, M.; Zhang, H.; Ding, W.
Data curation and Writing - original draft: Feng, Y.; Dai, J.; Wang, M.
Funding acquisition: Wan, J.; Xu, W.
Supervision, Validation and Writing, review & editing: Wan, J.

Availability of data and materials

Not applicable.

Acknowledgments

The authors acknowledge financial support from the National Natural Science Foundation of China (52203070). J. Wan expresses gratitude for the financial support provided by the China Scholarship Council (CSC) Visiting Scholar Program.

Conflicts of interest

All authors declared that there are no conflicts of interest.

Ethical approval and consent to participate

Not applicable.

Consent for publication

Not applicable.

REFERENCES

1. Sun, C.; Alonso, J. A.; Bian, J. Recent Advances in perovskite-type oxides for energy conversion and storage applications. *Adv. Energy. Mater.* **2021**, *11*, 2000459. DOI
2. Luo, D.; Li, X.; Dumont, A.; Yu, H.; Lu, Z. H. Recent progress on perovskite surfaces and interfaces in optoelectronic devices. *Adv. Mater.* **2021**, *33*, e2006004. DOI PubMed
3. Bui, T. H.; Shin, J. H. Perovskite materials for sensing applications: recent advances and challenges. *Microchem. J.* **2023**, *191*, 108924. DOI
4. Liu, Y.; Palotas, K.; Yuan, X.; et al. Atomistic origins of surface defects in $CH_3NH_3PbBr_3$ perovskite and their electronic structures. *ACS. Nano.* **2017**, *11*, 2060-5. DOI
5. Xian, J.; Jiang, H.; Wu, Z.; et al. Microwave shock motivating the Sr substitution of 2D porous $GdFeO_3$ perovskite for highly active oxygen evolution. *J. Energy. Chem.* **2024**, *88*, 232-41. DOI
6. Shin, S. S.; Lee, S. J.; Seok, S. I. Metal oxide charge transport layers for efficient and stable perovskite solar cells. *Adv. Funct. Mater.*

2019, *29*, 1900455. DOI

7. Hwang, J.; Rao, R. R.; Giordano, L.; Katayama, Y.; Yu, Y.; Shao-Horn, Y. Perovskites in catalysis and electrocatalysis. *Science* **2017**, *358*, 751-6. DOI PubMed
8. Sun, Q.; Yin, W. J. Thermodynamic stability trend of cubic perovskites. *J. Am. Chem. Soc.* **2017**, *139*, 14905-8. DOI PubMed
9. Zhang, F.; Park, S. Y.; Yao, C.; et al. Metastable Dion-Jacobson 2D structure enables efficient and stable perovskite solar cells. *Science* **2022**, *375*, 71-6. DOI
10. Buin, A.; Comin, R.; Xu, J.; Ip, A. H.; Sargent, E. H. Halide-dependent electronic structure of organolead perovskite materials. *Chem. Mater.* **2015**, *27*, 4405-12. DOI
11. Liu, G.; Gong, J.; Kong, L.; et al. Isothermal pressure-derived metastable states in 2D hybrid perovskites showing enduring bandgap narrowing. *Proc. Natl. Acad. Sci. U. S. A.* **2018**, *115*, 8076-81. DOI PubMed PMC
12. Mai, H.; Chen, D.; Tachibana, Y.; Suzuki, H.; Abe, R.; Caruso, R. A. Developing sustainable, high-performance perovskites in photocatalysis: design strategies and applications. *Chem. Soc. Rev.* **2021**, *50*, 13692-729. DOI
13. Deng, Z.; Ni, D.; Chen, D.; et al. Anti-perovskite materials for energy storage batteries. *InfoMat* **2022**, *4*, e12252. DOI
14. Jonderian, A.; Ting, M.; Mccalla, E. Metastability in Li-La-Ti-O perovskite materials and its impact on ionic conductivity. *Chem. Mater.* **2021**, *33*, 4792-804. DOI
15. Fu, Y.; Rea, M. T.; Chen, J.; et al. Selective Stabilization and photophysical properties of metastable perovskite polymorphs of $CsPbI_3$ in thin films. *Chem. Mater.* **2017**, *29*, 8385-94. DOI
16. Fan, M.; Guo, J.; Fang, G.; et al. Microwave-pulse assisted synthesis of tunable ternary-doped 2D molybdenum carbide for efficient hydrogen evolution. *Chem. Synth.* **2024**, *4*, 36. DOI
17. Shi, Y.; Zhou, Y.; Ma, Z.; Xiao, G.; Wang, K.; Zou, B. Structural regulation and optical behavior of three-dimensional metal halide perovskites under pressure. *J. Mater. Chem. C.* **2020**, *8*, 12755-67. DOI
18. Wu, Z.; Fan, M.; Jiang, H.; et al. Harnessing the unconventional cubic phase in 2D $LaNiO_3$ perovskite for highly efficient urea oxidation. *Angew. Chem. Int. Ed. Engl.* **2025**, *64*, e202413932. DOI
19. El-Ballouli, A. O.; Bakr, O. M.; Mohammed, O. F. Structurally tunable two-dimensional layered perovskites: from confinement and enhanced charge transport to prolonged hot carrier cooling dynamics. *J. Phys. Chem. Lett.* **2020**, *11*, 5705-18. DOI PubMed PMC
20. Sun, W.; Dacek, S. T.; Ong, S. P.; et al. The thermodynamic scale of inorganic crystalline metastability. *Sci. Adv.* **2016**, *2*, e1600225. DOI PubMed PMC
21. Wu, Z.; Xian, J.; Dai, J.; et al. Microwave-pulse synthesis of tunable 2D porous nickel-enriched $LaMnxNi_{1-x}O_3$ solid solution for efficient electrocatalytic urea oxidation. *J. Mater. Chem. A.* **2024**, *12*, 7047-57. DOI
22. Hong, Y.; Byeon, P.; Bak, J.; et al. Local-electrostatics-induced oxygen octahedral distortion in perovskite oxides and insight into the structure of Ruddlesden-Popper phases. *Nat. Commun.* **2021**, *12*, 5527. DOI PubMed PMC
23. Marronnier, A.; Roma, G.; Boyer-Richard, S.; et al. Anharmonicity and disorder in the black phases of cesium lead iodide used for stable inorganic perovskite solar cells. *ACS. Nano.* **2018**, *12*, 3477-86. DOI
24. Ning, M.; Wang, S.; Wan, J.; et al. Dynamic active sites in electrocatalysis. *Angew. Chem. Int. Ed. Engl.* **2024**, *63*, e202415794. DOI PubMed PMC
25. Ji, R.; Zhang, Z.; Hofstetter, Y. J.; et al. Perovskite phase heterojunction solar cells. *Nat. Energy.* **2022**, *7*, 1170-9. DOI
26. Jin, H.; Song, T.; Paik, U.; Qiao, S. Metastable two-dimensional materials for electrocatalytic energy conversions. *Acc. Mater. Res.* **2021**, *2*, 559-73. DOI
27. Jiang, H.; Li, J.; Xiao, Z.; et al. The rapid production of multiple transition metal carbides via microwave combustion under ambient conditions. *Nanoscale* **2020**, *12*, 16245-52. DOI
28. Ofoegbuna, T.; Peterson, B.; da, S. M. N.; et al. Modifying metastable $Sr_{1-x}BO_{3-\delta}$ (B = Nb, Ta, and Mo) perovskites for electrode materials. *ACS. Appl. Mater. Interfaces.* **2021**, *13*, 29788-97. DOI PubMed PMC
29. Yongfei, Y.; Guangyu, F.; Miao, F.; et al. Leveraging novel microwave techniques for tailoring the microstructure of energy storage materials. *Microstructures4*, 2024035. DOI
30. Wan, J.; Wu, Z.; Fang, G.; et al. Microwave-assisted exploration of the electron configuration-dependent electrocatalytic urea oxidation activity of 2D porous $NiCo_2O_4$ spinel. *J. Energy. Chem.* **2024**, *91*, 226-35. DOI
31. Li, B.; Zhang, Y.; Fu, L.; et al. Surface passivation engineering strategy to fully-inorganic cubic $CsPbI_3$ perovskites for high-performance solar cells. *Nat. Commun.* **2018**, *9*, 1076. DOI PubMed PMC
32. Wan, J.; Fang, G.; Mi, S.; et al. Metastable 2D amorphous Nb_2O_5 for aqueous supercapacitor energy storage. *Chem. Eng. J.* **2024**, *488*, 150912. DOI
33. Wan, J.; Hu, R.; Li, J.; et al. A universal construction of robust interface between 2D conductive polymer and cellulose for textile supercapacitor. *Carbohydr. Polym.* **2022**, *284*, 119230. DOI
34. Bartel, C. J.; Sutton, C.; Goldsmith, B. R.; et al. New tolerance factor to predict the stability of perovskite oxides and halides. *Sci. Adv.* **2019**, *5*, eaav0693. DOI PubMed PMC
35. Yao, H.; Zhao, J.; Li, Z.; Ci, Z.; Jin, Z. Research and progress of black metastable phase $CsPbI_3$ solar cells. *Mater. Chem. Front.* **2021**, *5*, 1221-35. DOI
36. Li, Q.; Fang, G.; Wu, Z.; et al. Advanced microwave strategies facilitate structural engineering for efficient electrocatalysis. *ChemSusChem* **2024**, *17*, e202301874. DOI
37. Hu, R.; Jiang, H.; Xian, J.; et al. Microwave-pulse sugar-blowing assisted synthesis of 2D transition metal carbides for sustainable

hydrogen evolution. *Appl. Catal. B-. Environ.* **2022**, *317*, 121728. DOI

38. Barone, C.; Lang, F.; Mauro, C.; et al. Unravelling the low-temperature metastable state in perovskite solar cells by noise spectroscopy. *Sci. Rep.* **2016**, *6*, 34675. DOI PubMed PMC
39. Varignon, J.; Bibes, M.; Zunger, A. Origin of band gaps in 3D perovskite oxides. *Nat. Commun.* **2019**, *10*, 1658. DOI PubMed PMC
40. Gao, B.; Liu, H.; Zhou, Z.; et al. An intriguing canting dipole configuration and its evolution under an electric field in La-doped Pb(Zr,Sn,Ti)O_3 perovskites. *Microstructures* **2022**, *2*, 2022010. DOI
41. Halder, S.; Sheikh, M. S.; Maity, R.; Ghosh, B.; Sinha, T. Investigating the optical, photosensitivity and photocatalytic properties of double perovskites A_2LuTaO_6 (A = Ba, Sr): a combined experimental and density functional theory study. *Ceram. Int.* **2019**, *45*, 15496-504. DOI
42. Basavarajappa, M. G.; Chakraborty, S. Rationalization of double perovskite oxides as energy materials: a theoretical insight from electronic and optical properties. *ACS. Mater. Au.* **2022**, *2*, 655-64. DOI PubMed PMC
43. He, R.; Wu, H.; Liu, S.; Liu, H.; Zhong, Z. Ferroelectric structural transition in hafnium oxide induced by charged oxygen vacancies. *Phys. Rev. B.* **2021**, 104. DOI
44. Liu, L.; Tang, Y.; Liu, S.; et al. Unraveling the trade-off between oxygen vacancy concentration and ordering of perovskite oxides for efficient lattice oxygen evolution. *Adv. Energy. Mater.* **2025**, *15*, 2402967. DOI
45. Navrotsky, A. Energetics and crystal chemical systematics among ilmenite, lithium niobate, and perovskite structures. *Chem. Mater.* **1998**, *10*, 2787-93. DOI
46. Ciccioli, A.; Latini, A. Thermodynamics and the intrinsic stability of lead halide perovskites $CH_3NH_3PbX_3$. *J. Phys. Chem. Lett.* **2018**, *9*, 3756-65. DOI PubMed
47. Fransson, E.; Rahm, J. M.; Wiktor, J.; Erhart, P. Revealing the free energy landscape of halide perovskites: metastability and transition characters in $CsPbBr_3$ and $MAPbI_3$. *Chem. Mater.* **2023**, *35*, 8229-38. DOI
48. Lopes, P. P.; Chung, D. Y.; Rui, X.; et al. Dynamically stable active sites from surface evolution of perovskite materials during the oxygen evolution reaction. *J. Am. Chem. Soc.* **2021**, *143*, 2741-50. DOI
49. Lyu, H.; Su, H.; Lin, Z. Two-stage dynamic transformation from δ- to α-$CsPbI_3$. *J. Phys. Chem. Lett.* **2024**, *15*, 2228-32. DOI
50. Makovec, D.; Križaj, N.; Meden, A.; et al. Ferroelectric bismuth-titanate nanoplatelets and nanowires with a new crystal structure. *Nanoscale* **2022**, *14*, 3537-44. DOI
51. Kim, H. J.; Kim, S. H.; Kim, S.; et al. Low-temperature crystallization of $LaFeO_3$ perovskite with inherent catalytically surface for the enhanced oxygen evolution reaction. *Nano. Energy.* **2023**, *105*, 108003. DOI
52. O'Donnell, S.; Kremer, R. K.; Maggard, P. A. Metastability and photoelectrochemical properties of Cu_2SnO_3 and $Cu_{2-x}Li_xTiO_3$: two Cu(I)-based oxides with delafossite structures. *Chem. Mater.* **2023**, *35*, 1404-16. DOI
53. Wang, Y.; Baldassarri, B.; Shen, J.; He, J.; Wolverton, C. Landscape of thermodynamic stabilities of $A_2BB'O_6$ compounds. *Chem. Mater.* **2024**, *36*, 6816-30. DOI
54. Yu, H.; Wan, J.; Goodsite, M.; Jin, H. Advancing direct seawater electrocatalysis for green and affordable hydrogen. *One. Earth.* **2023**, *6*, 267-77. DOI
55. Datta, K.; Neder, R. B.; Chen, J.; Neuefeind, J. C.; Mihailova, B. Atomic-level structural correlations across the morphotropic phase boundary of a ferroelectric solid solution: $xBiMg_{1/2}Ti_{1/2}O_3$-(1 - x)$PbTiO_3$. *Sci. Rep.* **2017**, *7*, 471. DOI PubMed PMC
56. Zhang, H.; Bi, Z.; Zhai, Z.; et al. Revealing unusual bandgap shifts with temperature and bandgap renormalization effect in phase-stabilized metal halide perovskite thin films. *Adv. Funct. Mater.* **2024**, *34*, 2302214. DOI
57. Asl H, Manthiram A. Proton-induced disproportionation of jahn-teller-active transition-metal ions in oxides due to electronically driven lattice instability. *J. Am. Chem. Soc.* **2020**, *142*, 21122-30. DOI PubMed
58. Klein, J.; Kampermann, L.; Mockenhaupt, B.; Behrens, M.; Strunk, J.; Bacher, G. Limitations of the tauc plot method. *Adv. Funct. Mater.* **2023**, *33*, 2304523. DOI
59. Nova, T. F.; Disa, A. S.; Fechner, M.; Cavalleri, A. Metastable ferroelectricity in optically strained $SrTiO_3$. *Science* **2019**, *364*, 1075-9. DOI PubMed
60. Li, X.; Qiu, T.; Zhang, J.; et al. Terahertz field-induced ferroelectricity in quantum paraelectric $SrTiO_3$. *Science* **2019**, *364*, 1079-82. DOI
61. Kim, J. R.; Jang, J.; Go, K. J.; et al. Stabilizing hidden room-temperature ferroelectricity via a metastable atomic distortion pattern. *Nat. Commun.* **2020**, *11*, 4944. DOI PubMed PMC
62. Kawamoto, T.; Fujita, K.; Yamada, I.; et al. Room-temperature polar ferromagnet $ScFeO_3$ transformed from a high-pressure orthorhombic perovskite phase. *J. Am. Chem. Soc.* **2014**, *136*, 15291-9. DOI
63. Zhang, X.; Pei, C.; Chang, X.; et al. FeO_6 octahedral distortion activates lattice oxygen in perovskite ferrite for methane partial oxidation coupled with CO_2 splitting. *J. Am. Chem. Soc.* **2020**, *142*, 11540-9. DOI
64. Gabilondo, E. A.; Newell, R. J.; Broughton, R.; et al. Switching lead for tin in $PbHfO_3$: noncubic structure of $SnHfO_3$. *Angew. Chem. Int. Ed. Engl.* **2024**, *63*, e202312130. DOI
65. Zhao, M.; Zhou, X.; Han, Y.; et al. Metastable γ-Li_2TiTeO_6: negative chemical pressure interception and polymorph tuning of SHG. *Chem. Mater.* **2022**, *34*, 10153-61. DOI
66. Zhao, M.; Zhu, C.; Sun, Z.; et al. Methodological approach to the high-pressure synthesis of nonmagnetic $Li_2B^{4+}B'^{6+}O_6$ oxides. *Chem. Mater.* **2022**, *34*, 186-96. DOI

67. Schlom, D. G.; Chen, L.; Pan, X.; Schmehl, A.; Zurbuchen, M. A. A thin film approach to engineering functionality into oxides. *J. Am. Ceram. Soc.* **2008**, *91*, 2429-54. DOI
68. O'donnell, S.; Chung, C.; Carbone, A.; Broughton, R.; Jones, J. L.; Maggard, P. A. Pushing the limits of metastability in semiconducting perovskite oxides for visible-light-driven water oxidation. *Chem. Mater.* **2020**, *32*, 3054-64. DOI
69. Dastidar, S.; Hawley, C. J.; Dillon, A. D.; Gutierrez-Perez, A. D.; Spanier, J. E.; Fafarman, A. T. Quantitative phase-change thermodynamics and metastability of perovskite-phase cesium lead iodide. *J. Phys. Chem. Lett.* **2017**, *8*, 1278-82. DOI PubMed
70. Gao, R.; Dong, Y.; Xu, H.; et al. Interfacial octahedral rotation mismatch control of the symmetry and properties of $SrRuO_3$. *ACS. Appl. Mater. Interfaces.* **2016**, *8*, 14871-8. DOI
71. Anderson, T. J.; Ryu, S.; Zhou, H.; et al. Metastable honeycomb $SrTiO_3$/$SrIrO_3$ heterostructures. *Appl. Phys. Lett.* **2016**, *108*, 151604. DOI
72. Jiang, Z.; Zhang, J.; Song, D.; et al. Metastable $SrRuO_3$ phases with lattice-dependent magnetic anisotropy by tailoring interfacial oxygen octahedral coupling. *Ceram. Int.* **2022**, *48*, 16825-31. DOI
73. Jaffe, A.; Mack, S. A.; Lin, Y.; Mao, W. L.; Neaton, J. B.; Karunadasa, H. I. High compression-induced conductivity in a layered Cu-Br perovskite. *Angew. Chem. Int. Ed. Engl.* **2020**, *59*, 4017-22. DOI
74. Ming, W.; Yang, D.; Li, T.; Zhang, L.; Du, M. H. Formation and diffusion of metal impurities in perovskite solar cell material $CH_3NH_3PbI_3$: implications on solar cell degradation and choice of electrode. *Adv. Sci. (Weinh).* **2018**, *5*, 1700662. DOI PubMed PMC
75. Shi, Y.; Chen, C.; Lou, Y.; Wang, Z. Strategies of perovskite mechanical stability for flexible photovoltaics. *Mater. Chem. Front.* **2021**, *5*, 7467-78. DOI
76. Zhou, G.; Jiang, X.; Zhao, J.; et al. Two-dimensional-layered perovskite $ALaTa_2O_7$:Bi^{3+} (A = K and Na) phosphors with versatile structures and tunable photoluminescence. *ACS. Appl. Mater. Interfaces.* **2018**, *10*, 24648-55. DOI
77. Pravarthana, D.; Lebedev, O. I.; David, A.; et al. Metastable monoclinic [110] layered perovskite $Dy_2Ti_2O_7$ thin films for ferroelectric applications. *RSC. Adv.* **2019**, *9*, 19895-904. DOI PubMed PMC
78. Shao, Z.; Saitzek, S.; Roussel, P.; Desfeux, R. Stability limit of the layered-perovskite structure in $Ln_2Ti_2O_7$ (Ln = lanthanide) thin films grown on (110)-oriented $SrTiO_3$ substrates by the sol-gel route. *J. Mater. Chem.* **2012**, *22*, 24894. DOI
79. Shao, Z.; Saitzek, S.; Ferri, A.; et al. Evidence of ferroelectricity in metastable $Sm_2Ti_2O_7$ thin film. *J. Mater. Chem.* **2012**, *22*, 9806. DOI
80. Katsumata, T.; Yamamoto, H.; Kimura, Y.; et al. Development of electrochemical anion doping technique for expansion of functional material exploration. *Adv. Funct. Materials.* **2023**, *33*, 2307116. DOI
81. Liu, R.; Si, L.; Niu, W.; et al. Light-induced mott-insulator-to-metal phase transition in ultrathin intermediate-spin ferromagnetic perovskite ruthenates. *Adv. Mater.* **2023**, *35*, e2211612. DOI
82. Waidha, A. I.; Zhang, H.; Lepple, M.; et al. $BaCoO_{2+}\delta$: a new highly oxygen deficient perovskite-related phase with unusual Co coordination obtained by high temperature reaction with short reaction times. *Chem. Commun. (Camb).* **2019**, *55*, 2920-3. DOI
83. Stoica, V. A.; Yang, T.; Das, S.; et al. Non-equilibrium pathways to emergent polar supertextures. *Nat. Mater.* **2024**, *23*, 1394-401. DOI
84. Kim, H.; Park, N. Importance of tailoring lattice strain in halide perovskite crystals. *NPG. Asia. Mater.* **2020**, *12*, 265. DOI
85. Jin, B.; Cao, J.; Yuan, R.; Cai, B.; Wu, C.; Zheng, X. Strain relaxation for perovskite lattice reconfiguration. *Adv. Energ. Sust. Res.* **2023**, *4*, 2200143. DOI
86. Navas, D.; Fuentes, S.; Castro-Alvarez, A.; Chavez-Angel, E. Review on sol-gel synthesis of perovskite and oxide nanomaterials. *Gels* **2021**, *7*, 275. DOI PubMed PMC
87. Lei, Y.; Xu, T.; Ye, S.; et al. Engineering defect-rich Fe-doped NiO coupled Ni cluster nanotube arrays with excellent oxygen evolution activity. *Appl. Catal. B-Environ.* **2021**, *285*, 119809. DOI
88. Zheng, L.; Nozariasbmarz, A.; Hou, Y.; et al. A universal all-solid synthesis for high throughput production of halide perovskite. *Nat. Commun.* **2022**, *13*, 7399. DOI PubMed PMC
89. Zeng, Y.; Szymanski, N. J.; He, T.; et al. Selective formation of metastable polymorphs in solid-state synthesis. *Sci. Adv.* **2024**, *10*, eadj5431. DOI PubMed PMC
90. Mueller, D. N.; De, S. R. A.; Yoo, H.; Martin, M. Phase stability and oxygen nonstoichiometry of highly oxygen-deficient perovskite-type oxides: a case study of $(Ba,Sr)(Co,Fe)O_{3-\delta}$. *Chem. Mater.* **2012**, *24*, 269-74. DOI
91. Falmbigl, M.; Karateev, I. A.; Golovina, I. S.; et al. Evidence of extended cation solubility in atomic layer deposited nanocrystalline $BaTiO_3$ thin films and its strong impact on the electrical properties. *Nanoscale* **2018**, *10*, 12515-25. DOI
92. Yamazoe, S.; Kawawaki, T.; Shibata, K.; Kato, K.; Wada, T. Synthetic mechanism of perovskite-type $KNbO_3$ by modified solid-state reaction process. *Chem. Mater.* **2011**, *23*, 4498-504. DOI
93. Usiskin, R. E.; Davenport, T. C.; Wang, R. Y.; Guan, W.; Haile, S. M. Bulk properties of the oxygen reduction catalyst $SrCo_{0.9}Nb_{0.1}O_{3-\delta}$. *Chem. Mater.* **2016**, *28*, 2599-608. DOI
94. Uusi-esko, K.; Karppinen, M. Extensive series of hexagonal and orthorhombic $RMnO_3$ (R = Y, La, Sm, Tb, Yb, Lu) thin films by atomic layer deposition. *Chem. Mater.* **2011**, *23*, 1835-40. DOI
95. Bora, T.; Al-hinai, M. H.; Al-hinai, A. T.; Dutta, J.; Jantzen, C. M. Phase transformation of metastable $ZnSnO_3$ upon thermal decomposition by *in-situ* temperature-dependent raman spectroscopy. *J. Am. Ceram. Soc.* **2015**, *98*, 4044-9. DOI
96. Xu, F.; Zou, Y.; Dai, Y.; Li, M.; Li, Z. Halide perovskites and high-pressure technologies: a fruitful encounter. *Mater. Chem. Front.* **2023**, *7*, 2102-19. DOI

97. Yamada, I.; Odake, T.; Asai, K.; et al. High-pressure synthesis of highly oxidized $Ba_{0.5}Sr_{0.5}Co_{0.8}Fe_{0.2}O_{3-\delta}$ cubic perovskite. *Mater. Chem. Front.* **2019**, *3*, 1209-17. DOI
98. Ishiwata, S.; Tokunaga, Y.; Taguchi, Y.; Tokura, Y. High-pressure hydrothermal crystal growth and multiferroic properties of a perovskite $YMnO_3$. *J. Am. Chem. Soc.* **2011**, *133*, 13818-20. DOI PubMed
99. Inaguma, Y.; Aimi, A.; Shirako, Y.; et al. High-pressure synthesis, crystal structure, and phase stability relations of a $LiNbO_3$-type polar titanate $ZnTiO_3$ and its reinforced polarity by the second-order Jahn-Teller effect. *J. Am. Chem. Soc.* **2014**, *136*, 2748-56. DOI
100. Fujita, K.; Kawamoto, T.; Yamada, I.; et al. $LiNbO_3$-type $InFeO_3$: room-temperature polar magnet without second-order Jahn-Teller active ions. *Chem. Mater.* **2016**, *28*, 6644-55. DOI
101. Khalyavin, D. D.; Salak, A. N.; Vyshatko, N. P.; et al. Crystal structure of metastable perovskite $Bi(Mg_{1/2}Ti_{1/2})O_3$: Bi-based structural analogue of antiferroelectric $PbZrO_3$. *Chem. Mater.* **2006**, *18*, 5104-10. DOI
102. Khalyavin, D. D.; Salak, A. N.; Fertman, E. L.; et al. The phenomenon of conversion polymorphism in Bi-containing metastable perovskites. *Chem. Commun. (Camb).* **2019**, *55*, 4683-6. DOI
103. Yan, L.; Niu, H.; Bridges, C. A.; et al. Unit-cell-level assembly of metastable transition-metal oxides by pulsed-laser deposition. *Angew. Chem. Int. Ed. Engl.* **2007**, *46*, 4539-42. DOI
104. Fan, X.; Lian, J.; Guo, Z.; Lu, H. Microstructure and photoluminescence properties of ZnO thin films grown by PLD on Si (111) substrates. *Appl. Surf. Sci.* **2005**, *239*, 176-81. DOI
105. Masood, K. B.; Kumar, P.; Malik, M. A.; Singh, J. A comprehensive tutorial on the pulsed laser deposition technique and developments in the fabrication of low dimensional systems and nanostructures. *Emergent. Mater.* **2021**, *4*, 737-54. DOI
106. Wu, X.; He, J.; Zhang, M.; et al. Binary Pd/amorphous-$SrRuO_3$ hybrid film for high stability and fast activity recovery ethanol oxidation electrocatalysis. *Nano. Energy.* **2020**, *67*, 104247. DOI
107. Schraknepper, H.; Bäumer, C.; Dittmann, R.; De, S. R. A. Complex behaviour of vacancy point-defects in $SrRuO_3$ thin films. *Phys. Chem. Chem. Phys.* **2015**, *17*, 1060-9. DOI PubMed
108. Langenberg, E.; Guzmán, R.; Maurel, L.; et al. Epitaxial stabilization of the perovskite phase in $(Sr_{1-x}Ba_x)MnO_3$ Thin Films. *ACS. Appl. Mater. Interfaces.* **2015**, *7*, 23967-77. DOI
109. Zhou, C.; Evans, C.; Dickey, E. C.; Rohrer, G. S.; Salvador, P. A. Epitaxial stabilization and persistent nucleation of the 3C polymorph of $Ba_{0.6}Sr_{0.4}MnO_3$. *ACS. Appl. Mater. Interfaces.* **2024**, *16*, 4873-85. DOI PubMed PMC
110. Wang, Q.; Gu, Y.; Chen, C.; Qiao, L.; Pan, F.; Song, C. Realizing metastable cobaltite perovskite via proton-induced filling of oxygen vacancy channels. *ACS. Appl. Mater. Interfaces.* **2023**, *15*, 1574-82. DOI
111. Chen, J.; Li, Z.; Dong, H.; et al. Pressure induced unstable electronic states upon correlated nickelates metastable perovskites as batch synthesized via heterogeneous nucleation. *Adv. Funct. Mater.* **2020**, *30*, 2000987. DOI
112. Enoch, C. M.; Ingavale, S.; Marbaniang, P.; Patil, I.; Swami, A. Molten salt-directed synthesis of strontium manganese perovskite oxide: an active electrocatalyst for the oxygen reduction reaction and oxygen evolution reaction. *J. Mater. Chem. A.* **2023**, *11*, 21780-92. DOI
113. Nikam, A. V.; Prasad, B. L. V.; Kulkarni, A. A. Wet chemical synthesis of metal oxide nanoparticles: a review. *Crystengcomm* **2018**, *20*, 5091-107. DOI
114. Muñoz, A.; Casáis, M. T.; Alonso, J. A.; et al. Complex magnetism and magnetic structures of the metastable homno3 perovskite. *Inorg. Chem.* **2001**, *40*, 1020-8. DOI
115. Yan, F.; Mi, Z.; Chen, J.; et al. Revealing the role of interfacial heterogeneous nucleation in the metastable thin film growth of rare-earth nickelate electronic transition materials. *Phys. Chem. Chem. Phys.* **2022**, *24*, 9333-44. DOI
116. Li, X.; Li, Z.; Yan, F.; et al. Batch synthesis of rare-earth nickelates electronic phase transition perovskites via rare-earth processing intermediates. *Rare. Met.* **2022**, *41*, 3495-503. DOI
117. O'donnell, S.; Osborn, D. J.; Krishnan, G.; et al. Prediction and kinetic stabilization of Sn(II)-perovskite oxide nanoshells. *Chem. Mater.* **2022**, *34*, 8054-64. DOI
118. Liu, L.; Zhang, Q.; Wang, Y.; Yan, Z.; Hou, Z. Li-doped $(K,Na)NbO_3$ particles with high crystallinity and chemical stability synthesized by molten salt method. *Advanced. Powder. Technology.* **2024**, *35*, 104580. DOI
119. Börgers, J. M.; De, S. R. A. The surprisingly high activation barrier for oxygen-vacancy migration in oxygen-excess manganite perovskites. *Phys. Chem. Chem. Phys.* **2020**, *22*, 14329-39. DOI PubMed
120. Lee, S. A.; Ok, J. M.; Lee, J.; et al. Epitaxial stabilization of metastable 3C $BaRuO_3$ thin film with ferromagnetic non-fermi liquid phase. *Adv. Elect. Mater.* **2021**, *7*, 2001111. DOI
121. Song, Y. H.; Ge, J.; Mao, L. B.; et al. Planar defect-free pure red perovskite light-emitting diodes via metastable phase crystallization. *Sci. Adv.* **2022**, *8*, eabq2321. DOI PubMed PMC
122. Ding, J.; Zhu, X. Research progress on quadruple perovskite oxides. *J. Mater. Chem. C.* **2024**, *12*, 9510-61. DOI
123. Hu, R.; Wei, L.; Xian, J.; et al. Microwave shock process for rapid synthesis of 2D porous $La_{0.2}Sr_{0.8}CoO_3$ perovskite as an efficient oxygen evolution reaction catalyst. *Acta. Physico-Chimica. Sinica.* **2023**, *39*, 221202. DOI
124. Jiang, H.; Xian, J.; Hu, R.; et al. Microwave discharge for rapid introduction of bimetallic-synergistic configuration to conductive catecholate toward long-term supercapacitor. *Chem. Eng. J.* **2023**, *455*, 140804. DOI